Banner appropriate to article type will appear here in typeset article

Effect of rotation on wake vortices in stratified flow

Jinyuan Liu[1], Pranav Puthan[1],and Sutanu Sarkar[1,2,]†

[1]Mechanical and Aerospace Engineering, University of California San Diego, La Jolla, CA 92093, USA

[2]Scripps Institution of Oceanography, La Jolla, CA 92037, USA

(Received xx; revised xx; accepted xx)

Stratified wakes past an isolated conical seamount are simulated at a Froude number of $Fr = 0.15$ and Rossby numbers of $Ro = 0.15$, 0.75, and ∞. The wakes exhibit a Kármán vortex street, unlike their unstratified, non-rotating counterpart. Vortex structures are studied in terms of large-scale global modes, as well as spatially localised vortex evolution, with a focus on rotation effects. The global modes are extracted by spectral proper orthogonal decomposition (SPOD). For all three studied Ro ranging from mesoscale, submesoscale, and non-rotating cases, the frequency of the SPOD modes at different heights remains coupled as a global constant. However, the shape of the SPOD modes changes from slanted 'tongues' at zero rotation ($Ro = \infty$) to tall hill-height columns at strong rotation ($Ro = 0.15$). A novel method for vortex centre tracking shows that, in all three cases, the vortices at different heights advect uniformly at about $0.9U_\infty$ beyond the near wake, consistent with the lack of variability of the global modes. Under system rotation, cyclonic vortices (CVs) and anticyclonic vortices (AVs) present considerable asymmetry, especially at $Ro = 0.75$. The vorticity distribution as well as the stability of AVs are tracked downstream using statistics conditioned to the identified vortex centres. At $Ro = 0.75$, intense AVs with relative vorticity up to $\omega_z/f_c = -2.4$ are seen with small regions of instability but all AVs evolve towards a more stable state. Recent stability analysis that accounts for stratification and viscosity is found to improve on earlier criteria.

Key words: Rotating flows; stratified flows; wakes; vortex dynamics;

1. Introduction

The planet that we live on is full of multi-scale eddies, generated by various sources ranging from uneven thermal energy distribution at the largest scales, wind-driven ocean surface motions, to relatively more localised obstacle-induced flows. The dynamics of such eddies are greatly enriched by incorporating stratification, rotation, and turbulence. Understanding these dynamics is essential to geophysics. This work will be focused particularly on the last example – wake eddies generated by obstacles.

In the deep ocean, seamounts and hills are stirring rods; they induce vortical motion, turbulence, and internal gravity waves, which enhance heat and mass transport and hence

† Email address for correspondence: ssarkar@ucsd.edu

crucially impact the ocean state. In the atmosphere, mountains commonly trigger wakes and waves, and orographic lifting is a source of convective weather, including air unsteadiness, formation of cumulonimbus clouds, and precipitation. Both the ocean and the atmosphere are stratified, and the scales of motions are large enough to feel the effect of Earth's rotation, leading to distinctive wake dynamics. The understanding of the wakes behind three-dimensional (3D) obstacles from a fluid dynamics perspective would benefit the modelling and prediction of the multi-scale motions of oceanic and atmospheric bottom boundary flows.

In this study, we consider the wake of a steady uni-directional mean flow (U_∞) perturbed by an isolated conical seamount/hill submerged in the fluid (figure 1). The background has stable density stratification that is linear so that the buoyancy frequency $N = \sqrt{-g\partial_z\bar{\rho}/\rho_0}$ is a constant. The Coriolis frequency $f_c = 2\Omega_c$ is a negative constant (Southern hemisphere). The conical obstacle, which has base diameter D, height h, and slope of 30°, is placed on a flat bottom wall.

Two non-dimensional numbers, the vertical Froude number ($Fr = U_\infty/Nh$) and the Rossby number ($Ro = U_\infty/|f_c|D$) are the main controlling parameters. An additional (but not independent) non-dimensional number, the Burger number ($Bu = N^2h^2/f_c^2D^2 = (Ro/Fr)^2$) that characterises the importance of stratification relative to rotation will also be used.

Stratified hill wakes have been studied extensively through laboratory experiments, field observations, and numerical simulations. Hunt & Snyder (1980) showed experimentally, that for relatively strong stratification ($Fr < 0.4$), there is a potential energy barrier below which the flow does not have sufficient kinetic energy to go over the hill and, instead, flows around the hill to form a quasi-two-dimensional (Q2D) Kármán vortex shedding (VS) pattern. This is a significant qualitative difference between stratified and unstratified flow past a three-dimensional obstacle. Without stratification, the flow goes over the obstacle and horseshoe structures are formed (Garcia-Villalba *et al.* 2009). Castro *et al.* (1983) showed in stratified flow past a finite-span ridge that, as Fr decreases from above to below unity, the wake behind the hill transitions from a lee-wave-dominated regime to a vortex-dominated regime, with the latter regime being the focus of this work. They found that at or below $Fr = 0.2$ (their figure 7, last row), the modulation of the vortex wake by the lee waves can be neglected except near the peak of the ridge. Boyer *et al.* (1987) studied experimentally the effect of system rotation on stratified hill wakes in the regime of $Ro = O(0.1)$, $Fr = O(0.1)$-$O(1)$, equivalently $Bu = O(1)$-$O(10)$ variation. They found that the VS frequency is not strongly affected by changing Ro. However, the Reynolds number ($Re_D < 1200$) was not sufficient for the wake to be turbulent. For non-rotating hill wakes, Vosper *et al.* (1999) varied the Froude number and the shape of the wake generator, and found that the VS frequency is a weak increasing function of Fr, and the St-Fr relationships collapses for different object shapes if the reference velocity is corrected for blockage. More recently, Teinturier *et al.* (2010); Lazar *et al.* (2013*b*) performed laboratory experiments on the LEGI-Coriolis platform at moderate-to-high Reynolds number ($Re_D \sim O(10^3)$-$O(10^4)$) that featured the asymmetry between cyclonic and anticyclonic vortices generated behind a towed cylinder tank.

In terms of field observations, island wakes have acquired much attention recently and wakes have been studied near Palau (MacKinnon *et al.* 2019; Zeiden *et al.* 2021), the Green Island off the coast of Taiwan (Chang *et al.* 2019), and in the lee of Guadalupe (Horvath *et al.* 2020), to name a few. A strong sign of a narrow-band VS mode stood out from the broadband turbulence signal. Those observations were made in *in situ* conditions that have the complications of irregular terrain, tidal motion, and nonlinear stratification, but the amount of data – both in space and in time – is insufficient for a more comprehensive study of the spatio-temporal structure of the wake. This limitation along with the possibility of a

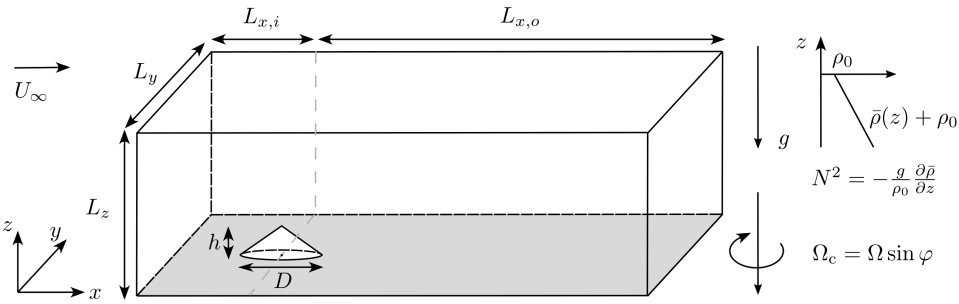

FIGURE 1. Flow configuration (not to scale). The background density is linearly stratified. The frame is rotating at a constant angular velocity $\Omega_c = \Omega \sin\varphi$, where Ω is the Earth's angular velocity and φ is the latitude. The Coriolis frequency, $f_c = 2\Omega_c$, is negative. Gravity, density stratification and the axis of rotation all point to negative $\hat{z}$.

controlled parametric study motivates our high-fidelity numerical simulations in an idealized setting.

For rotating stratified hill wakes, numerical studies include the utilization of the hydrostatic regional oceanic modelling system (ROMS) (Shchepetkin & McWilliams 2005), such as Dong *et al.* (2007); Perfect *et al.* (2018); Perfect (2019); Srinivasan *et al.* (2021); Jagannathan *et al.* (2021), and the hydrostatic version of the MIT-GCM model (Marshall *et al.* 1997*b*,*a*), such as Liu & Chang (2018).

Recently, Puthan *et al.* (2021, 2022*a*,*b*) conducted large-eddy simulation (LES) of stratified hill wakes without the hydrostatic approximation. The focus was on the role of tidal modulation of a mean current in a regime with weak rotational effects. The findings included tidal synchronization (vortex shedding at specific tidal subharmonics that depend on the tidal excursion number), phases with enhanced turbulent dissipation, and higher form drag. A similar numerical procedure will be followed in this work while excluding the periodic tide and focussing on rotation effects.

The susceptibility of the flow to rotation can be categorised according to the characteristic Rossby number ($Ro = U/(|f_c|D) = (U/D)/|f_c|$), which is the ratio of rotation timescale to the advection timescale. When $O(Ro) \ll 1$, rotation is fast enough to establish a geostrophic balance between Coriolis force and pressure gradient. Such is the case with mesoscale motion or the even larger general circulation. When $O(Ro) \gg 1$, advective nonlinearity evolves flow structures before they feel the presence of rotation. This regime is categorized as small-scale stratified flow. When $O(Ro) \sim 1$, the flow is away from geostrophic balance, but rotation is equally important as advection and able to affect the flow. With a typical order-unity Rossby number, and a length scale in physical space of $O(100\,\mathrm{m}) \sim O(10\,\mathrm{km})$, submesoscale dynamics (Taylor & Thompson 2023) has been an increasingly popular topic in geophysical fluid dynamics, oceanography, and meteorology.

In this paper, we present results from seamount/hill wakes at $Fr = 0.15$ and three representative Rossby numbers, $Ro = 0.15, 0.75, \infty$, corresponding to mesoscale, submesoscale, and non-rotating stratified flow regimes, respectively. There is near-wake turbulence but our focus will be on the coherent wake vortices that are found beyond the near wake.

The rest of the paper is structured as follows: Section 2 introduces the numerical methods and the LES simulations conducted as part of this work; section 3 elucidates the global structures in the flow that are coherent in space and time via flow visualisations and spectral proper orthogonal decomposition (SPOD); section 4 presents ensemble-averaged tracks of the centres of vortices that are obtained by application of a pattern recognition method;

section 5 is a systematic study of the asymmetry between and instabilities of cyclones and anticyclones; section 6 concerns the evolution of the mean momentum wake; and, finally, section 7 is a summary and discussion of the results.

2. Numerical simulations

The incompressible Navier-Stokes equations are solved in a Cartesian coordinate with x, y, and z being the streamwise, transverse, and vertical directions, as shown in figure 1. In the momentum equation, density variation appears only in the buoyancy as per the Boussinesq approximation and system rotation is represented by the Coriolis force. The dimensional governing equations in index notation are as follows:

$$\frac{\partial u_i}{\partial x_i} = 0, \tag{2.1}$$

$$\frac{\partial u_i}{\partial t} + \frac{\partial u_i u_j}{\partial x_j} - f_c \epsilon_{ij3}(u_j - U_\infty \delta_{j1}) = -\frac{1}{\rho_0}\frac{\partial p^*}{\partial x_i} + \frac{\partial \tau_{ij}}{\partial x_j} - \frac{\rho^* g}{\rho_0}\delta_{i3}, \tag{2.2}$$

$$\frac{\partial \rho}{\partial t} + \frac{\partial \rho u_i}{\partial x_i} = \frac{\partial J_{\rho,i}}{\partial x_i}, \tag{2.3}$$

$$\tau_{ij} = (\nu + \nu_{\mathrm{sgs}})(\frac{\partial u_i}{\partial x_j} + \frac{\partial u_j}{\partial x_i}),\ J_{\rho,i} = (\kappa + \kappa_{\mathrm{sgs}})\frac{\partial \rho}{\partial x_i}. \tag{2.4}$$

The total density ρ is decomposed into the reference density ρ_0, the background density $\bar{\rho}(z)$, and the density perturbation ρ^* due to fluid motion,

$$\rho(x, y, z, t) = \rho_0 + \bar{\rho}(z) + \rho^*(x, y, z, t). \tag{2.5}$$

The total pressure is written as

$$p(x, y, z, t) = p_0 + p_g(y) + p_a(z) + p^*(x, y, z, t), \tag{2.6}$$

where the reference pressure p_0 is a constant, the hydrostatic (ambient) pressure p_a has a vertical gradient that balances the ambient density ($\rho_a = \rho_0 + \bar{\rho}(z)$), and the geostrophic pressure p_g has a transverse gradient that balances the Coriolis force due to the velocity U_∞ of the freestream. Only the dynamic pressure p^* appears in the momentum equation (2.2).

The LES is performed at a moderately high Reynolds number $Re_D = U_\infty D/\nu = 10\,000$. Spatial derivatives are discretized with a second-order central finite difference on a staggered grid, and the equations are advanced in time using a combined scheme with third-order Runge-Kutta for the convection terms and Crank-Nicolson for the diffusion terms. Continuity is enforced by solving the pressure Poisson equation. The obstacle is represented by an immersed boundary method (Balaras 2004; Yang & Balaras 2006). The subgrid-scale model is chosen to be the WALE model (Nicoud & Ducros 1999) with the sub-grid-scale Prandtl number $Pr = \mu_{\mathrm{sgs}}/\kappa_{\mathrm{sgs}}$ set to unity. For more numerical details, the reader is referred to Puthan *et al.* (2020).

The computational domain spans a volume of $L_x \times L_y \times L_z = [-4, 15] \times [-4, 4] \times [0, 4]$ in units of D and the horizontal resolution of the immersed body and the turbulent near wake ($-1 < x/D < 2$) is held constant at $(\Delta x, \Delta y) \approxeq (0.003D, 0.006D) \leqslant (4\eta, 8\eta)$, with a mild stretching in the streamwise direction. Here η is the minimum Kolmogorov length scale at the centerline at different heights. The vertical resolution below $z/h = 1.2$ is kept at $\Delta z = 0.008h \approxeq 0.05U_\infty/N$ to resolve the length scale for vertical overturning motion U_∞/N.

The inflow condition is a uniform velocity inlet, and the outflow is a Neumann-type convective outlet. The lateral boundaries are periodic to reduce the blockage effect and to

Case	Bu	Ro	Fr	(N_x, N_y, N_z)	N_t	TU_∞/D	color code
BuInf	∞	∞				295	red
Bu25	25	0.75	0.15	(1536,1280,320)	4000	345	green
Bu1	1	0.15				322	blue

TABLE 1. Parameters of simulated cases. N_x, N_y, and N_z are the number of grid points in each direction and N_t is the total number of available snapshots that will be used for all statistics. T is the time span of the stored data.

allow the wake to flap. The top boundary is shear free, and the bottom boundary is modelled by a quadratic drag law as in Puthan *et al.* (2020); Jagannathan *et al.* (2021). The drag coefficient is chosen as $c_D = 0.002$ in common with oceanography applications (Haidvogel & Beckmann 1999; Arbic & Scott 2008). Its value was validated in a stratified bottom Ekman layer by Taylor & Sarkar (2008) and tested in stratified flow over complex geometry by Rapaka & Sarkar (2016), among others. Sponge layers are placed at the inlet and the top boundaries to reduce spurious reflected internal wakes. The overall numerical setting was validated by Puthan *et al.* (2020, 2021).

The parameter space explored is shown in table 1. The stratification is held constant at $Fr = 0.15$, a typical value for midsize topography in the ocean and the atmosphere, and is in the 'flow-around' regime where coherent wake vortices dominate. Meanwhile, the rotation Rossby number is varied as $Ro = 0.15, 0.75, \infty$, to study its effect on the vortex wake. These three values of Ro correspond to mesoscale, submesoscale, and non-rotating geophysical flows. The induced Burger number are $Bu = 1, 25, \infty$, which will be used to label different cases.

We compile a time-resolved numerical database that consists of three rotation strengths and collect the data after statistical stationarity is reached. Each case has $N_t = 4000$ snapshots that span around 300 convective time units ($T = 300D/U_\infty$), which corresponds to roughly 80 VS periods. Statistics, to be discussed later, are obtained by averaging over the entire interval, T.

3. Large-scale coherent structures

In geophysical flows, coherent vortical structures are commonly observed. There is no universal definition of coherent structures, but they are generally strong enough and have relatively independent dynamics to distinguish themselves from the background flow, account for a significant portion of the fluctuation energy of the system, are spatially organized, and their lifetime is sufficient for them to be dynamically important. The wake eddies of this paper have the aforementioned features.

Large-scale Kármán vortices, a specific type of coherent structure, are associated with vortex shedding from bluff bodies. In geophysical applications, they are commonly found in flows impinging on bottom or side topography, e.g. island wakes (Young & Zawislak 2006; Chang *et al.* 2019; Horvath *et al.* 2020), headland wakes (Pawlak *et al.* 2003), and in laboratory flows (Hunt & Snyder 1980; Castro *et al.* 1983; Boyer *et al.* 1987; Teinturier *et al.* 2010), among others. In field observations and laboratory experiments, the features of the coherent vortices are inferred from single- or multiple-point statistics and flow visualizations. The data is limited in spatial coverage and resolution.

In what follows, coherent structures will be studied in two ways. First, individual snapshots in which vortex structures are vividly visible are used for a qualitative overview of rotation effects (section 3.1). Second, a more comprehensive quantitative assessment is obtained

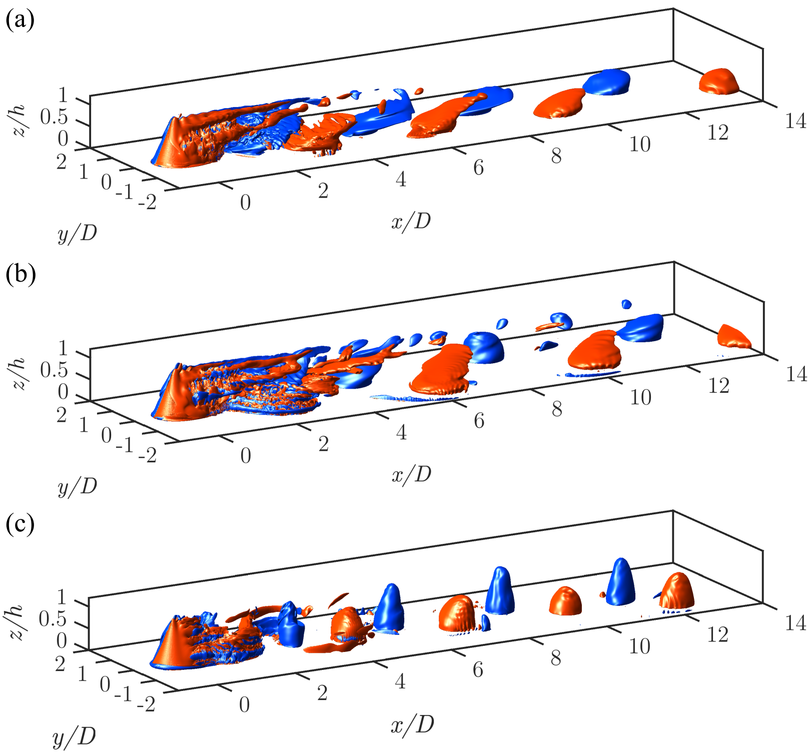

FIGURE 2. Visualisation of the isosurfaces of $|\omega_z|D/U_\infty = 1.5, 1.0, 3.0$ for BuInf, Bu25, and Bu1 (top to bottom), respectively. Red and blue indicate positive (anticyclonic since f_c is negative) and negative (cyclonic) vorticity, respectively. Note the vertical axis is normalised with the height h of the hill, which is about 0.3 times the base diameter D.

by applying SPOD to the time-resolved LES database in table 1 to reveal the statistical significance of the coherent structures. Section 3.2 reviews the theory and implementation of SPOD, followed by the analysis of the temporal eigenspectra (section 3.3) and spatial modes (section 3.4).

3.1. *Flow visualisations*

A first impression of the 3D spatial organization of the wake vortices is provided by the isosurfaces of the vertical component of vorticity ($\omega_z = (\nabla \times \boldsymbol{u})_z$) in figure 2(a-c) for cases BuInf, Bu25, and Bu1, respectively.

In the near-wake region ($x/D < 3$), the ω_z isosurface is space-filling and multiscale, indicating greater turbulence intensity than further downstream. But after $x/D = 3$, the vortices quickly organise into spatially compact coherent structures that persist to the end of the computational domain with little change. Rotation clearly influences the shape and size of the structures. For case BuInf in figure 2(a), the structures are slanted 'tongues' with horizontal dimensions greater than their height. As the strength of rotation is increased, the horizontal size shrinks and the height increases as in figure 2(b) for Bu25. With further increase of rotation, the vortex structures become aligned with the vertical axis, appearing as tall 'columns' that extend from the flat bottom to the hill height, in figure 2(c).

The wake vortices are composed of cyclones (rotation is in the same direction as that of the frame) and anticyclones. It is found in figure 2(b,c) that, with the presence of rotation, the

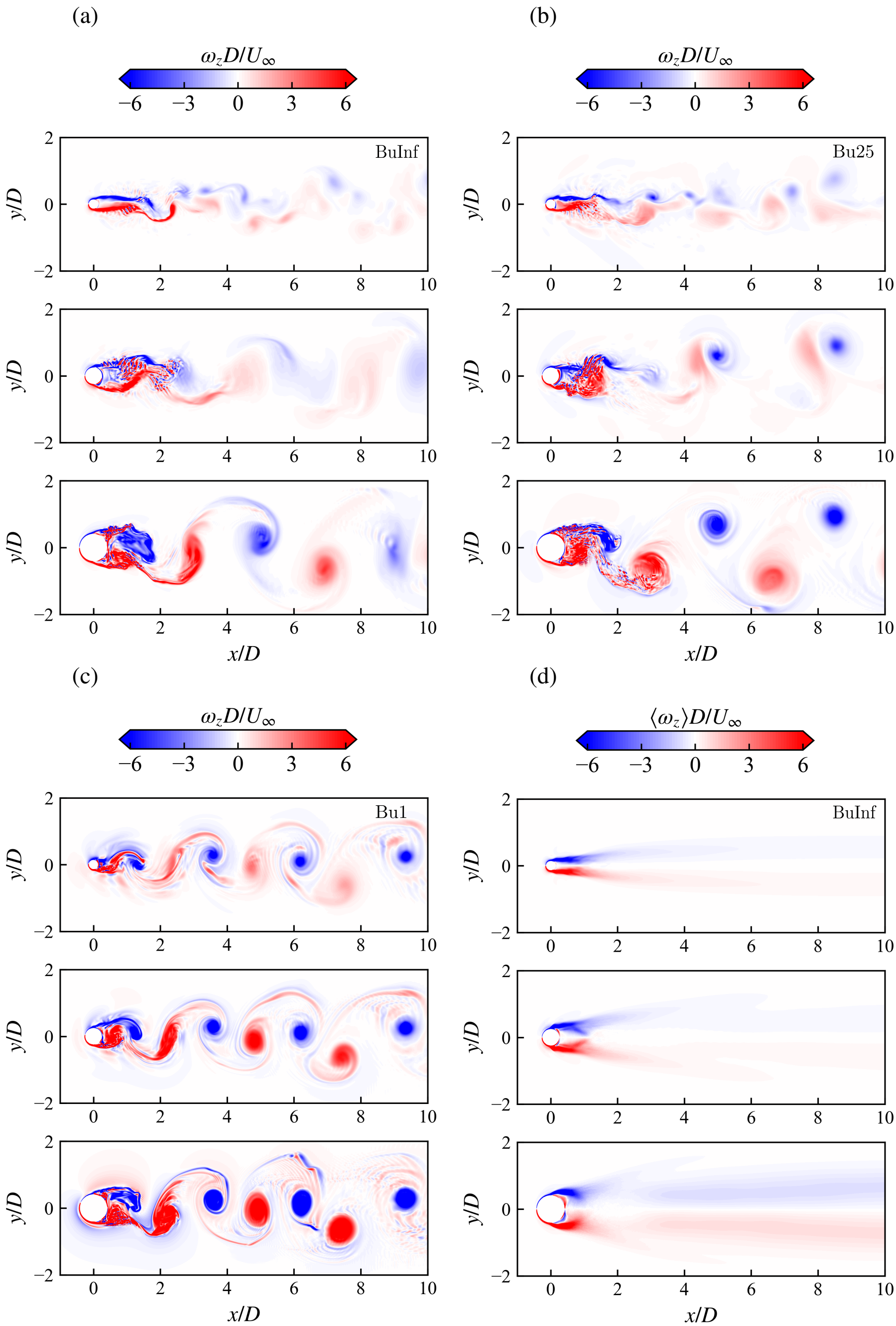

FIGURE 3. (a,b,c) Instantaneous and (d) time-averaged ω_z at horizontal planes at $z/h = 0.75, 0.50, 0.12$ (from top to bottom in each subfigure). (a,d) Cases BuInf, (b) Bu25, (c) Bu1.

cyclones (negative vortices in blue) are different from anticyclones (positive vortices in red) with regards to size, shape, and vorticity distribution as will be elaborated in later sections.

In figure 2(c), cyclones are taller and thinner than anticyclones and, as will be shown, have stronger interior vorticity.

Figure 3(a,b,c) show the instantaneous ω_z at several heights for all three cases. In all three cases, a pattern of Q2D Kármán vortices is distinct in all planes at $z/h = 0.12, 0.25, 0.75$. The flow is akin to a vortex wake rather than its unstratified counterpart of a three-dimensional turbulent wake (Garcia-Villalba *et al.* 2009).

The mean vertical vorticity ($\langle\omega_z\rangle$) of case BuInf is shown in figure 3(d). For the lower two planes, the mean looks very similar to those obtained in low Reynolds number two-dimensional cylinder wakes, such as in Barkley (2006); Mittal (2008), both at $Re_D = 100$. Such similarity supports the Q2D feature of the hill wake at $Fr = 0.15$. At the same time, there is a notable difference: the flow in each horizontal place that cuts the hill *does not* represent an independent two-dimensional (2D) flow around a cylinder with the local hill diameter. Among different planes at different heights in figure 3(d), the length of the attached shear layer (with dark colors), is approximately a constant, regardless of the variation of the local hill diameter. This is consistent with the fact that the VS frequency is a *global constant* which will be discussed in detail in the next section, as the shear layer length is correlated to the shedding frequency (Williamson & Brown 1998).

In the SPOD analysis of the next section, the vertical vorticity on different horizontal planes ($\omega_z(x, y, t; z)$) is chosen as the quantity of interest since the large-scale wake structures involve predominantly Q2D vortical motion (figures 2-3), the shedding and evolution processes of which are well represented by ω_z. Moreover, the focus of this work is on the influence of increasing rotation strength on the horizontal motion, which tends to constrain the flow to be around the vertical axis at the large scales and significantly enhance ω_z as will be shown later. In the rotating cases Bu25 and Bu1, the stability of the anticyclones will also be studied (section 5) with ω_z being one of the most important metrics, hence we apply ω_z rather than other vortex identification criteria for overall consistency.

As seen in figures 2-3, ω_z structures exhibit dissimilar vertical organisation at different levels of rotation, although Kármán vortices are present in each horizontal plane. Owing to stratification, a vertical length scale of $U_\infty/N = Frh = 0.15h$ is introduced to the flow, and whether vortex structures remain coherent over vertical distances larger than U_∞/N regardless of rotation (suggested affirmatively by figure 2) needs quantitative investigation. To that end, we perform SPOD on vertically offset horizontal planes at $z/h = 0.12, 0.25, 0.50, 0.75$ ($N_x \times N_y \times N_z = 1538 \times 1280 \times 1$) and the vertical center plane at $y = 0$ ($N_x \times N_y \times N_z = 1538 \times 1 \times 320$) to allow the choice of different dominant (vortex shedding) frequencies at different heights by the flow and avoid imposing *a priori* a global frequency.

3.2. *Spectral POD and its numerical implementation*

Proper orthogonal decomposition (POD) is a matrix-factorization-based modal decomposition of complex systems introduced into fluid mechanics by Bakewell Jr & Lumley (1967); Lumley (1967, 1970).

Consider a statistically stationary square-integrable multi-variable signal $\boldsymbol{q}(\boldsymbol{x}, t) \in \mathcal{L}^2_{\boldsymbol{W}}(\boldsymbol{\Omega})$ with zero mean. Here $\mathcal{L}^2_{\boldsymbol{W}}$ is the Hilbert space equipped with a weighted inner product

$$(\boldsymbol{q}_1, \boldsymbol{q}_2)_{\boldsymbol{W}} = \int_{\boldsymbol{\Omega}} \boldsymbol{q}_2^{\mathrm{H}}(\boldsymbol{x})\, \boldsymbol{W}(\boldsymbol{x}) \boldsymbol{q}_1(\boldsymbol{x})\, \mathrm{d}\boldsymbol{x} \tag{3.1}$$

on a bounded domain $\boldsymbol{\Omega}$, and $(\cdot)^{\mathrm{H}}$ denotes Hermitian transpose. The weight matrix $\boldsymbol{W}$ is Hermitian positive-definite and the weighted 2-norm is defined as $\|\boldsymbol{q}_1\|_{\boldsymbol{W}} = (\boldsymbol{q}_1, \boldsymbol{q}_1)^{1/2}_{\boldsymbol{W}}$. The symbol $\langle\cdot\rangle_{\mathrm{E}}$ denotes the ensemble average over all realizations, and it is equivalent to the time average under ergodicity. The goal of POD is to find an empirical function $\boldsymbol{\psi}(\boldsymbol{x})$ that solves the optimization problem

$$\boldsymbol{\psi}(\boldsymbol{x}) = \arg \max_{\|\boldsymbol{\psi}\|_{\boldsymbol{W}}=1} \langle(\boldsymbol{q}, \boldsymbol{\psi})_{\boldsymbol{W}}\rangle_{\mathrm{E}}, \tag{3.2}$$

which defines $\boldsymbol{\psi}(\boldsymbol{x})$ as the function on which the projection of $\boldsymbol{q}(\boldsymbol{x}, t)$ is maximized in the sense of the least squares. Since $\mathcal{L}^2_{\boldsymbol{W}}$ is an infinite-dimensional space, a practical way to obtain the empirical function $\boldsymbol{\psi}(\boldsymbol{x})$ is to approximate it within a finite-dimensional space spanned by $\{\boldsymbol{\psi}^{(i)}\}_{i=1}^{M}$, where $\boldsymbol{\psi}^{(i)}$ is the i-th spatial mode and M is the order of truncation. It was shown in Holmes *et al.* (2012) that the optimization problem (3.2) can be converted to a Fredholm eigenvalue problem as

$$\mathcal{R}\boldsymbol{\psi}^{(i)}(\boldsymbol{x}) = \int_{\Omega} \boldsymbol{R}(\boldsymbol{x}, \boldsymbol{x}')\boldsymbol{W}(\boldsymbol{x}')\boldsymbol{\psi}^{(i)}(\boldsymbol{x}')\,\mathrm{d}\boldsymbol{x}' = \lambda^{(i)}\boldsymbol{\psi}^{(i)}(\boldsymbol{x}), \tag{3.3}$$

where $\mathcal{R}$ is a linear operator and $\boldsymbol{R}(\boldsymbol{x}, \boldsymbol{x}') = \langle\boldsymbol{q}(\boldsymbol{x})\boldsymbol{q}^{\mathrm{H}}(\boldsymbol{x}')\rangle_{\mathrm{E}}$ is the two-point correlation tensor. Since $\boldsymbol{R}$ is Hermitian positive-definite, its eigenvalues $\lambda^{(i)}$ are real positive that each represents a fraction of the fluctuation energy, and the eigenvectors $\{\boldsymbol{\psi}^{(i)}\}_{i=1}^{M}$ form an orthogonal basis under the inner product (3.1).

In the framework of spectral POD (SPOD), the eigenvalue problem (3.3) is cast as

$$\mathcal{R}\boldsymbol{\psi}^{(i)}(\boldsymbol{x}, t) = \int_{\Omega}\int_{-\infty}^{\infty} \boldsymbol{R}(\boldsymbol{x}, \boldsymbol{x}', t, t')\boldsymbol{W}(\boldsymbol{x}')\boldsymbol{\psi}^{(i)}(\boldsymbol{x}', t')\,\mathrm{d}\boldsymbol{x}'\mathrm{d}t' = \lambda^{(i)}\boldsymbol{\psi}^{(i)}(\boldsymbol{x}, t), \tag{3.4}$$

and $\boldsymbol{R}(\boldsymbol{x}, \boldsymbol{x}', t, t') = \langle\boldsymbol{q}(\boldsymbol{x}, t)\boldsymbol{q}^{\mathrm{H}}(\boldsymbol{x}', t')\rangle_{\mathrm{E}}$ is the two-point, two-time correlation tensor. With time-homogeneity, it reduces to $\boldsymbol{R}(\boldsymbol{x}, \boldsymbol{x}', \tau)$ as a function of $\tau = t - t'$, and is the Fourier transform pair of the spectral density tensor $\boldsymbol{S}(\boldsymbol{x}, \boldsymbol{x}', f) = \langle\hat{\boldsymbol{q}}(\boldsymbol{x}, f)\hat{\boldsymbol{q}}^{\mathrm{H}}(\boldsymbol{x}', f)\rangle_{\mathrm{E}}$:

$$\boldsymbol{R}(\boldsymbol{x}, \boldsymbol{x}', \tau) = \int_{-\infty}^{\infty} \boldsymbol{S}(\boldsymbol{x}, \boldsymbol{x}', f)e^{i2\pi f\tau}\,\mathrm{d}f. \tag{3.5}$$

Hence, $\boldsymbol{\phi}^{(i)}(\boldsymbol{x}, f) = \boldsymbol{\psi}^{(i)}(\boldsymbol{x}, t)e^{-i2\pi f\tau}$ will be the corresponding eigenmodes of the following eigenvalue problem

$$\mathcal{S}\boldsymbol{\phi}^{(i)}(\boldsymbol{x}, f) = \int_{\Omega} \boldsymbol{S}(\boldsymbol{x}, \boldsymbol{x}', f)\boldsymbol{W}(\boldsymbol{x}')\boldsymbol{\phi}^{(i)}(\boldsymbol{x}', f)\,\mathrm{d}\boldsymbol{x}' = \lambda^{(i)}(f)\boldsymbol{\phi}^{(i)}(\boldsymbol{x}, f), \tag{3.6}$$

which will be solved separately for each frequency. Here $\hat{\boldsymbol{q}}(\boldsymbol{x}, f)$ denotes the Fourier mode of $\boldsymbol{q}(\boldsymbol{x}, t)$ at frequency f, and can be represented by the eigenfunctions $\boldsymbol{\phi}^{(i)}(\boldsymbol{x}, f)$ as

$$\hat{\boldsymbol{q}}(\boldsymbol{x}, f) = \sum_{i=1}^{\infty} \sqrt{\lambda^{(i)}(f)}\boldsymbol{\phi}^{(i)}(\boldsymbol{x}, f). \tag{3.7}$$

In the occasion of spectral POD, the weighted inner-product in (3.1)-(3.2) will be a space-time integral

$$(\boldsymbol{q}_1, \boldsymbol{q}_2)_{\boldsymbol{W}} = \int_{\Omega}\int_{-\infty}^{\infty} \boldsymbol{q}_2^{\mathrm{H}}(\boldsymbol{x}, t)\boldsymbol{W}(\boldsymbol{x})\boldsymbol{q}_1(\boldsymbol{x}, t)\,\mathrm{d}\boldsymbol{x}\mathrm{d}t. \tag{3.8}$$

We note that at the same frequency f, different eigenvectors $\boldsymbol{\phi}^{(i)}(\boldsymbol{x}, f), \boldsymbol{\phi}^{(j)}(\boldsymbol{x}, f)$ are orthogonal under the spatial inner product (3.1) due to the symmetric positive-definiteness of $\boldsymbol{S}(\boldsymbol{x}, \boldsymbol{x}', f)$. But eigenvectors $\boldsymbol{\phi}^{(i)}(\boldsymbol{x}, f_1), \boldsymbol{\phi}^{(i)}(\boldsymbol{x}, f_2)$ at the same rank (i) associated with different frequencies are not necessarily orthogonal under space-only inner product.

Our numerical implementation is similar to those in Towne *et al.* (2018); Schmidt & Colonius (2020). Data are sampled into blocks of sequenced snapshots (shown below is the l-th block)

$$\boldsymbol{Q}^{(l)} = [\boldsymbol{q}_1^{(l)}, \boldsymbol{q}_2^{(l)}, ..., \boldsymbol{q}_{N_{\mathrm{FFT}}}^{(l)}] \in \mathbb{R}^{N_d \times N_{\mathrm{FFT}}}, \tag{3.9}$$

where each column $\boldsymbol{q}_i^{(l)}$ is one snapshot. The total number of snapshots in one block (ensemble) is N_{FFT}. The degree of freedom of one snapshot is $N_d = N_x \times N_y \times N_z \times N_{\mathrm{var}}$, where N_{var} is the dimension of the vector $\boldsymbol{q}(\boldsymbol{x}, t)$. In this study, we apply SPOD on the vertical component of vorticity (ω_z, hence $N_{\mathrm{var}} = 1$) in horizontal and vertical two-dimensional cross-sections of the flow (with either $N_z = 1$ or $N_y = 1$, respectively).

A discrete Fourier transform (DFT) is performed on each block $\boldsymbol{Q}^{(l)}$ to yield

$$\hat{\boldsymbol{Q}}^{(l)} = [\hat{\boldsymbol{q}}_1^{(l)}, \hat{\boldsymbol{q}}_2^{(l)}, \dots, \hat{\boldsymbol{q}}_{N_{\mathrm{FFT}}}^{(l)}] \in \mathbb{C}^{N_d \times N_{\mathrm{FFT}}}. \tag{3.10}$$

Then the Fourier modes are sorted according to frequency (labeled as the k-th discrete frequency) to form

$$\hat{\boldsymbol{Q}}_k = [\hat{\boldsymbol{q}}_k^{(1)}, \hat{\boldsymbol{q}}_k^{(2)}, \dots, \hat{\boldsymbol{q}}_k^{(N_{\mathrm{blk}})}] \in \mathbb{C}^{N_d \times N_{\mathrm{blk}}}. \tag{3.11}$$

The sampled spectral density at the k-th frequency is then $\boldsymbol{S}_k = \hat{\boldsymbol{Q}}_k \hat{\boldsymbol{Q}}_k^{\mathrm{H}} / (N_{\mathrm{blk}} - 1)$ and the discrete form of the eigenvalue problem (3.6) is

$$\boldsymbol{S}_k \boldsymbol{W} \boldsymbol{\Phi}_k = \boldsymbol{\Phi}_k \boldsymbol{\Lambda}_k, \tag{3.12}$$

with the weight matrix $\boldsymbol{W}$ containing the weights of numerical quadrature at each grid point. In practice, (3.12) is typically solved with the method of snapshots of Sirovich (1987) by replacing $\boldsymbol{\Phi}_k = \hat{\boldsymbol{Q}}_k \boldsymbol{\Psi}_k$ such that (3.12) becomes an equivalent eigenvalue problem

$$\frac{1}{N_{\mathrm{blk}} - 1} \hat{\boldsymbol{Q}}_k^{\mathrm{H}} \boldsymbol{W} \hat{\boldsymbol{Q}}_k \boldsymbol{\Psi}_k = \boldsymbol{\Psi}_k \boldsymbol{\Lambda}_k. \tag{3.13}$$

that has a much smaller dimension when $N_{\mathrm{blk}} \ll N_d$ is true. Hence, the eigenmodes of $\boldsymbol{S}_k$ are recovered as $\tilde{\boldsymbol{\Phi}}_k = \hat{\boldsymbol{Q}}_k \boldsymbol{\Psi}_k \boldsymbol{\Lambda}_k^{-1/2}$ such that the eigenvalue decomposition is

$$\boldsymbol{S}_k = \tilde{\boldsymbol{\Phi}}_k \boldsymbol{\Lambda}_k \tilde{\boldsymbol{\Phi}}_k^{\mathrm{H}} = \sum_{i=1}^{N_{\mathrm{blk}}} \lambda_k^{(i)} \tilde{\boldsymbol{\phi}}_k^{(i)} (\tilde{\boldsymbol{\phi}}_k^{(i)})^{\mathrm{H}}. \tag{3.14}$$

The physical meaning of the spatial modes $\tilde{\boldsymbol{\Phi}}_k(\boldsymbol{x})$ can be interpreted as either the eigenvector of the spectral density tensor $\boldsymbol{S}_k$ or the left singular vector of the Fourier mode $\hat{\boldsymbol{q}}_k$, at a discrete frequency f_k.

SPOD takes advantage of extracting spatial modes that evolve at a single frequency from a time-resolved database as in table 1. It was applied to analyse stratified wakes by Nidhan *et al.* (2020, 2022), who showed that it can successfully extract the large-scale VS motions and the associated characteristic frequency. In oceanography applications, Zeiden *et al.* (2021) applied a similar approach called empirical orthogonal functions (EOF) therein to the flow past an island and successfully separated the vortical modes and the tidal modes. But in their case, the EOFs are fit to three mooring points instead of the bulk of the flow, hence are different from ours where the eigenmodes will be emphasised as global modes.

When converting the time series into Fourier modes in (3.10), Welch's method (Welch 1967) is used to reduce the variance of the spectrum, with $N_{\mathrm{FFT}} = 512$ snapshots in each block, and a Hamming window on each block to enforce periodicity. An overlap ratio of 50% ($N_{\mathrm{ovlp}} = 256$) between two sequential blocks is chosen to offset the effect of low weights near the edges of the window. We end up with 13 blocks and the ensemble average will be taken over all blocks to obtain SPOD eigenspectra. The convergence of the method is checked via reducing the frequency resolution to $N_{\mathrm{FFT}} = 256$, or reducing the total number of snapshots from $N_t = 4000$ to 3000, and 2000. A high confidence level is obtained for the largest six eigenvalues as well as the sum of all eigenvalues, at each frequency. This follows the fact that for general eigenvalue-revealing algorithms, large eigenvalues converge faster. And it is noted that, in the present wakes, converging high-rank SPOD eigenvalues with much smaller magnitudes is still challenging even with $N_t = 4000$ snapshots. In this paper, no particular analysis will be conducted for higher than the sixth eigenvalue at any frequency.

In this database, a constant maximal Courant–Friedrichs–Lewy (CFL) number is kept during the simulation, which results in an uneven (but almost uniform) time spacing of snapshots. To obtain uniformly spaced data for DFT, a piecewise cubic Hermite interpolation (PCHIP) is performed in time.

3.3. *SPOD eigenspectra and vortex shedding frequencies*

Figure 4(a-c) shows the global vertical enstrophy spectra $S_{\omega_z\omega_z}(f)$ at different 2D planes for BuInf, Bu25, and Bu1, respectively. The spectral density at a discrete frequency f_k is computed by summing over all SPOD eigenvalues at this frequency:

$$S_{\omega_z\omega_z}(f_k) = \sum_{i}^{N_{\mathrm{blk}}} \lambda^{(i)}(f_k) = \mathrm{tr}(\boldsymbol{S}_k \boldsymbol{W}) = \int_{\boldsymbol{\Omega}} \boldsymbol{S}(\boldsymbol{x}, \boldsymbol{x}, f_k)\, \mathrm{d}\boldsymbol{x}, \tag{3.15}$$

and is the spectral density of the area-integrated squared ω_z. It is independent of SPOD.

For all three cases and all planes examined, the spectra display strong harmonic spikes, with the strongest peak defined as the VS frequency (f_{VS}) in each plane. The VS frequency is independent of the vertical location of the four horizontal planes, and is also the same in the central vertical plane, even though performing SPOD on separate planes allows the freedom of selecting different frequencies. This indicates that for each case, f_{VS} is a global constant (for the heights examined), and the VS modes are three-dimensional global modes. The VS Strouhal number is $St_{\mathrm{VS}} = f_{\mathrm{VS}} D/U_\infty = 0.264, 0.249, 0.266$ for BuInf, Bu25, and Bu1, respectively. It is noted that, since the characteristic frequency of the global mode (f_{VS}) does not depend on the height or the local hill diameter, normalising it with a different length scale than the hill base diameter D would just make St_{VS} different by a scalar multiple. However, as will be discussed later, the numerical values of St_{VS} using D correspond well to that of vortex shedding from a circular cylinder. Also, since D determines the size of the largest scales in the flow, it is a natural choice for the normalizing scale. In the eigenspectra, the successive peaks are harmonics of the VS frequency at $2St_{\mathrm{VS}}$, $3St_{\mathrm{VS}}$, and so on.

Perfect *et al.* (2018) found that whether the VS frequency is a global constant or is controlled by the local hill diameter, depends on a non-dimensional parameter: Burger number (Bu). The Burger number characterises the relative importance of two counteracting mechanisms for vertical coupling: rotation and stratification. When Bu is small (rotation is strong), the bulk of the flow adjusts to be around the axis of rotation quickly, and geostrophic balance is established, where the vertical variation is minimized. As Bu is increased, the vertical intercommunication is progressively weakened by stratification. Perfect *et al.* (2018) use the diameter at half-height to be the characteristic horizontal scale so that their values of Rossby number (Ro^*) and Burger number (Bu^*) are related to our values by $Ro^* = 2Ro$ and $Bu^* = 4Bu$. They performed a number of simulations and found that $Bu^*_{\mathrm{cri}} = 5.5$, equivalently $Bu_{\mathrm{cri}} = 1.4$, is a regime-separation criterion below which the rotation is strong enough to couple different layers to form vertically aligned vortices. Also, when $Bu^* > 12$, equivalently $Bu > 3$, they found stratification to be more prominent so that vortices are shed at different layers relatively independently. Turning to the present results, in each of the cases at $Fr = 0.15$ whose Ro span unity to infinity, the VS frequency is independent of height, indicating a potential disagreement between Perfect *et al.* (2018) and our results. On the other hand, for Froude numbers similar to $Fr = 0.15$ in Perfect *et al.* (2018), almost all the cases (see figure 4, therein) were labeled as ‘vertically coupled shedding’ and had strong rotation with Ro between 0.025 and 0.25. Only their weakest rotation case with $Ro = 0.25$

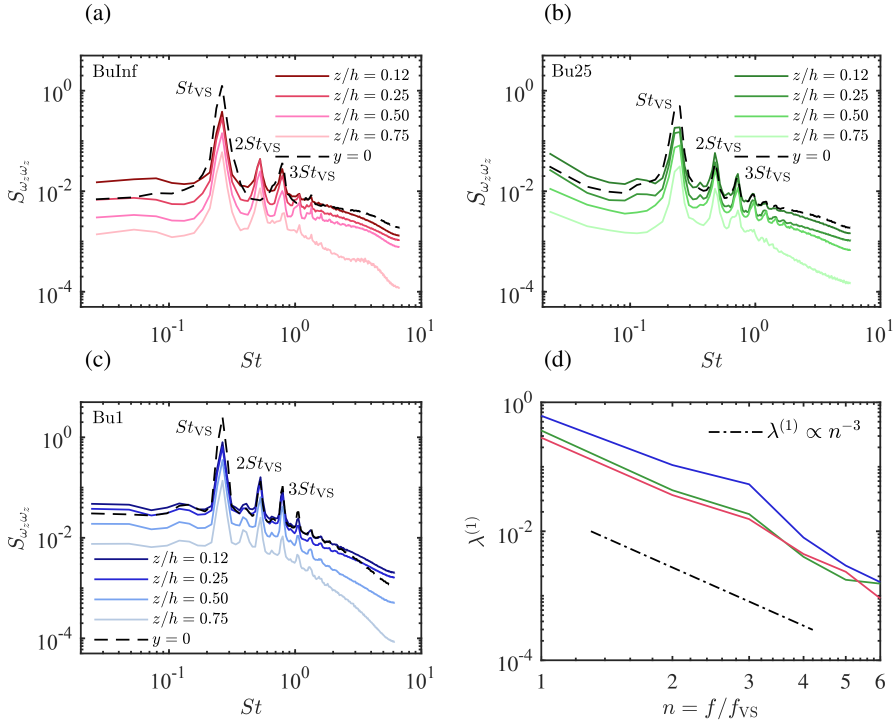

FIGURE 4. (a-c) Global power spectra $S_{\omega_z\omega_z}$ of ω_z as a function of Strouhal number ($St = fD/U_\infty$). Spectra are shown at four horizontal planes $z/h = 0.12, 0.25, 0.50, 0.75$, and the central vertical plane at $y = 0$. The VS Strouhal number is marked as St_{VS} as well as the VS harmonics. The values take $St_{\mathrm{VS}} = 0.264, 0.249$, and 0.266 in (a-c), for cases BuInf, Bu25, and Bu1, respectively. (d) Decay of the largest eigenvalue at the VS frequency f_{VS} and the harmonics (indexed by $n = f/f_{\mathrm{VS}}$) for the horizontal plane $z/h = 0.25$ (results are similar for other locations). Color codes same as in (a-c).

was labeled as 'vertically decoupled shedding'. It is also worth noting that, in the ROMS simulations, vertical motions and pressure correlations are quite approximate (specially in the near wake where vortex shedding is accompanied by small-scale turbulence) since the momentum equation in that direction is reduced to a hydrostatic balance, and the pressure field might play an important role in coupling VS.

Nevertheless, the fact that the modes extracted by SPOD are global modes, and they evolve at the same frequency, implies that the large-scale vortices at $Fr = 0.15$ are horizontally and vertically coherent, as opposed to layered dynamics in strongly stratified flows. Our findings indicate that the stratification of $Fr = 0.15$ is not strong enough to vertically decouple the vortex dynamics in the wake of the conical seamount, regardless of the presence of rotation, and inclusion of Fr is necessary in addition to Bu. The pure Burger number criterion has the limitation that, for instance, with no rotation and small stratification, Bu will be far larger than Bu_{cri} but the VS frequency can still be a global constant. The Fr that marks the transition from vertically coupled to decoupled VS in non-rotating hill wakes is subject to future research.

Boyer *et al.* (1987) studied experimentally the wake behind a conical obstacle in linearly stratified rotating flows. Their parameters spanned $0.08 < Fr < 0.28$, $0.06 < Ro < 0.4$, and for three Reynolds numbers $Re_D = 380, 760, 1140$. Based on the measurement on single horizontal cross-sections, they found the VS Strouhal number to be only a weak

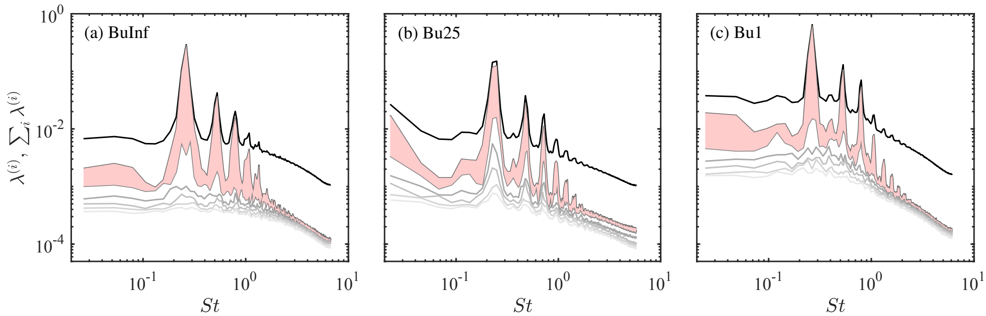

FIGURE 5. SPOD eigenspectra: (a) BuInf, (b) Bu25, and (c) Bu1. Horizontal plane at $z/h = 0.25$ is shown (results are similar for other locations). From top to bottom are the summation of all eigenvalues (darkest, spectral density as in figure 4(a-c)), and the first to the sixth eigenvalues (from dark to light: $i = 1, 2, 3, 4, 5, 6$), as a function of Strouhal number ($St = fD/U_\infty$). The difference between the first and the second eigenvalue is filled with color.

function of both Re and Ro. The robustness of the VS frequency to rotation strength is also observed numerically in this work, in a similar Fr-Ro regime but at a turbulent Reynolds number $Re_D = 10\,000$. Even though their Strouhal numbers are measured as the vortex advection velocity divided by the mean separation of two same sign vortices, and ranged from $0.20 < St < 0.35$, our VS Strouhal numbers still present a good quantitative agreement with theirs. Moreover, we interpret the VS frequency revealed by SPOD as the characteristic frequency of the most energetic global mode, which also agrees with single-point frequency measurements in the intermediate wake ($x/D > 3$, not shown).

The values of St_{VS} for all three cases are close to $St = 0.2665$, which is the $Re \to \infty$ asymptote of the St-Re relationship in low Reynolds number 2D cylinder wakes proposed by (Williamson & Brown 1998). Note that their relation $St = 0.2665 - 1.018\sqrt{Re}$ is given for $50 < Re_D < 180$ which is before the transition to 3D wakes. This transition happens at around $Re = 188.5$ according to a global Floquet instability of the periodic wake (Barkley & Henderson 1996). As a result, the St-Re relationship experiences a discontinuity as a sudden jump of St during this transition (Williamson & Brown 1998; Fey *et al.* 1998), and the asymptote of $St = 0.2665$ isn't reached in three-dimensional cylinder wakes. Fey *et al.* (1998) showed that the maximum VS Strouhal number in a cylinder wake of about $St = 0.21$ is reached right before the onset of the Kelvin-Helmholtz instability in the shear layer. We interpret the observed values of VS frequencies in our hill wakes as a saturation of the Q2D VS, which won't be observed in three-dimensional cylinder wakes at this Reynolds number and above. This interpretation is consistent with the finding in Boyer *et al.* (1987) that the robustness of f_{VS} to rotation rate is not affected by the Reynolds number, in their low-to-moderate Reynolds number experiments.

The enstrophy distribution among different eigenvalues is an important measure of the complexity of the system. Figure 5 shows the sum of all eigenvalues, and also the first to the sixth eigenvalues (from dark to light) according to their absolute value. For frequencies at or close to the VS frequency and its harmonics, the first eigenvalue accounts for most of the enstrophy, and is an order of magnitude larger than the second eigenvalue. However, for larger frequencies ($St > 2$), the dominance of the leading eigenvalues is lost, as the degree of freedom for small-scale motions is increased. The significance of low-rankness in the spectra is therefore two-fold. There are strong harmonic spikes in the SPOD eigenspectra in figure 4(a-c), implying that a great portion of enstrophy is contained in the large-scale VS motions.

For the VS shedding frequency and its harmonics, the first two eigenvalues contribute the most of the enstrophy.

Moreover, the enstrophy distribution among the harmonics is shown in figure 4(d). The decay of the first eigenvalue $\lambda^{(1)}$ as a function of the integer harmonic index $n = f/f_{VS}$ is plotted. Similar to figure 5, one horizontal plane $z/h = 0.25$ is chosen, but the results are qualitatively similar for the other three selected horizontal planes. For all three Burger numbers, $\lambda^{(1)}$ decays approximately as a power progression as n^{-3}, which is slower than the geometric decay of distinct POD eigenvalues in 2D cylinder wakes (Noack *et al.* 2003). Nevertheless, higher harmonics contain a progressively smaller amount of enstrophy. Additionally, by comparing the absolute value of $\lambda^{(1)}$ in figure 4(d) and $\sum_i \lambda^{(i)}$ in figure 4(a-c), it is generally true that vertical enstrophy is increased as the rotating rate increases. This is an effect of system rotation that promotes vortical motion around the rotation axis as will be discussed in more detail in section 5.

In all, the large scales of the vortical motion can be well represented by a few characteristic frequencies and the associated leading modes. Such low-rank behaviour suggests the possibility of reduced-order modelling of stratified hill wakes even at large Reynolds numbers.

3.4. *SPOD eigenfunctions and large-scale global modes*

Apart from the temporal characteristics uncovered by SPOD eigenspectra, the SPOD eigenmodes represent energetic flow structures that are coherent in space and time and, therefore, dynamically important. The real parts of the leading SPOD modes (corresponding to the largest eigenvalue at each frequency) are plotted in figures 6-7, for two frequencies f_{VS} and $2f_{VS}$ and on various 2D planes. The eigenfunctions are free up to a scalar multiple and are normalised by the largest modulus of the spatial mode in the same plane. The interpretation of the magnitude of the eigenmodes (or the darkness of the colors) as the intensity of the structures is only meaningful when the comparison is made within the same plane.

For case BuInf (no rotation), the VS mode in figure 6(a) is reminiscent of the marginally stable global modes found in the linear stability analysis of low Reynolds number cylinder wakes (Barkley & Henderson 1996; Mittal 2008). However, the phases of the global mode are different in different planes, with the phases of higher planes leading. This is clearer in the vertical plane ($y = 0$), which shows the tilting and elongation of the structures as an effect of stratification. Note that the vertical coordinate is normalised by the hill height h which is about 0.3 times the base diameter; in un-normalized coordinates, the angle of the slanted 'tongues' is very shallow. The tilting angle from the horizontal of the structures in the top panel of figure 6(a) ranges from about 8° close to the bottom wall to 2° near the top, with an average of about 4° which is almost constant during the evolution. Although the VS structures are not vertical, they still evolve cohesively at f_{VS} and experience little change during the advection. In the later section 4, the lack of change of the tilting angle will be shown to be a result of a roughly constant advection velocity of the vortices. Similar slanted mode as in figure 6(a) was found in a stratified sphere wake by Chongsiripinyo *et al.* (2017) (referred as 'surfboards' therein), but whether it is a common feature of stratified bluff-body wakes is subject to future research.

Moreover, the standing-wave-like spatial modes of f_{VS} in figure 6(a) are symmetric about $y = 0$, representing the advection of the perturbation vorticity $\omega_z' = \omega_z - \langle\omega_z\rangle$. The projection of ω_z' on the f_{VS} mode has a period of T_{VS} and the streamwise wavelength of the mode is interpreted as the average spacing of the Kármán vortices. The appearance of the symmetric f_{VS} mode on the antisymmetric mean flow (see figure 3d), in analogy to low Reynolds number 2D cylinder wakes (Kumar & Mittal 2006), can be viewed as an accompaniment to the symmetry-breaking bifurcation from a steady wake to periodic shedding.

The modes of $2f_{VS}$ in figure 6(b) are antisymmetric, with a wavelength about half of

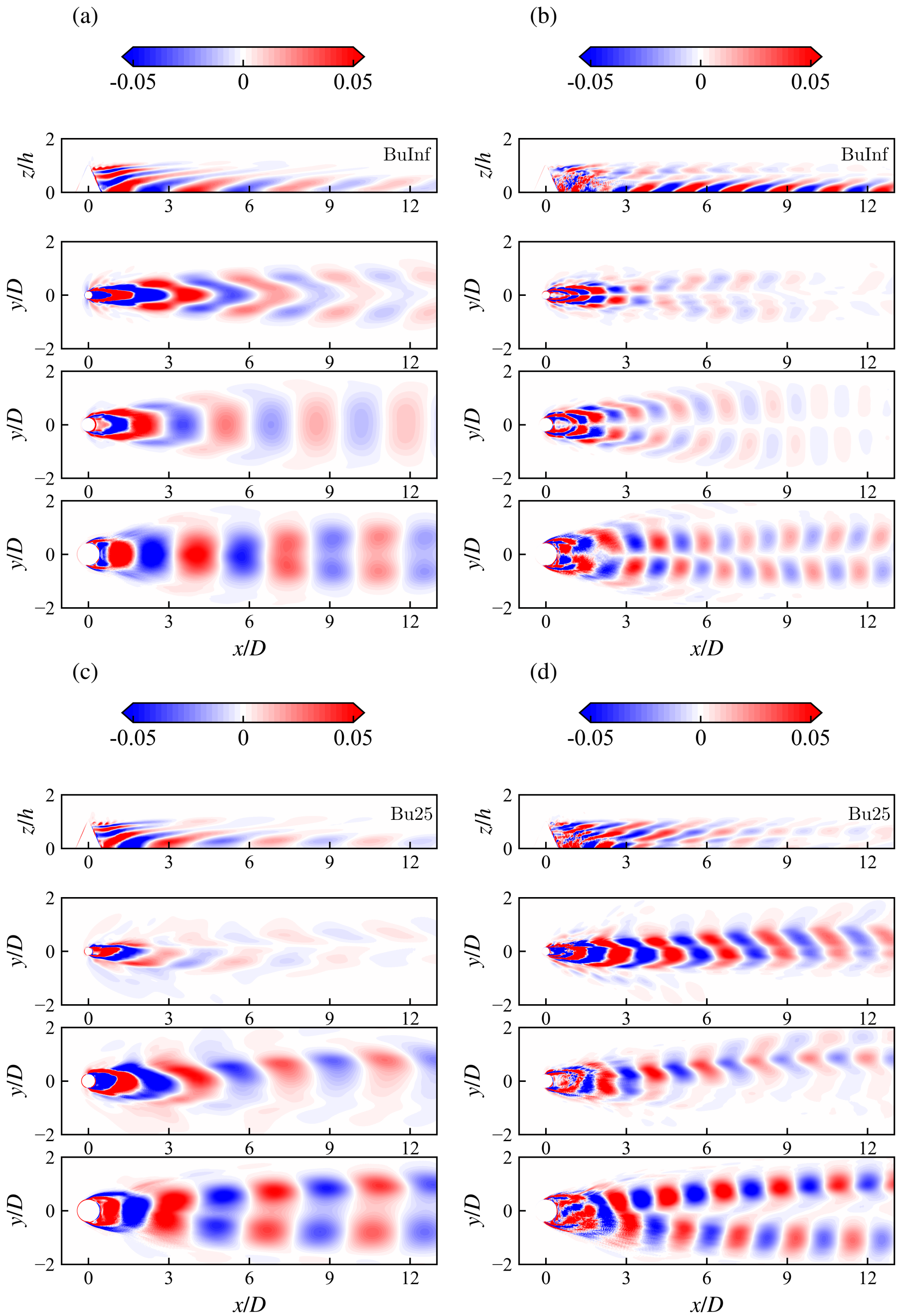

FIGURE 6. Leading SPOD eigenmodes corresponding to f_{VS} (a,c) and $2f_{\mathrm{VS}}$ (b,d), for cases BuInf (a,b) and Bu25 (c,d). The plotted quantity is the real part of SPOD eigenfunction on each plane, normalized by the maximum value in the plane. In each figure, the top plane is a vertical plane is at $y = 0$, and the lower planes are, from the second row to bottom, horizontal planes at $z/h = 0.75, 0.50, 0.12$.

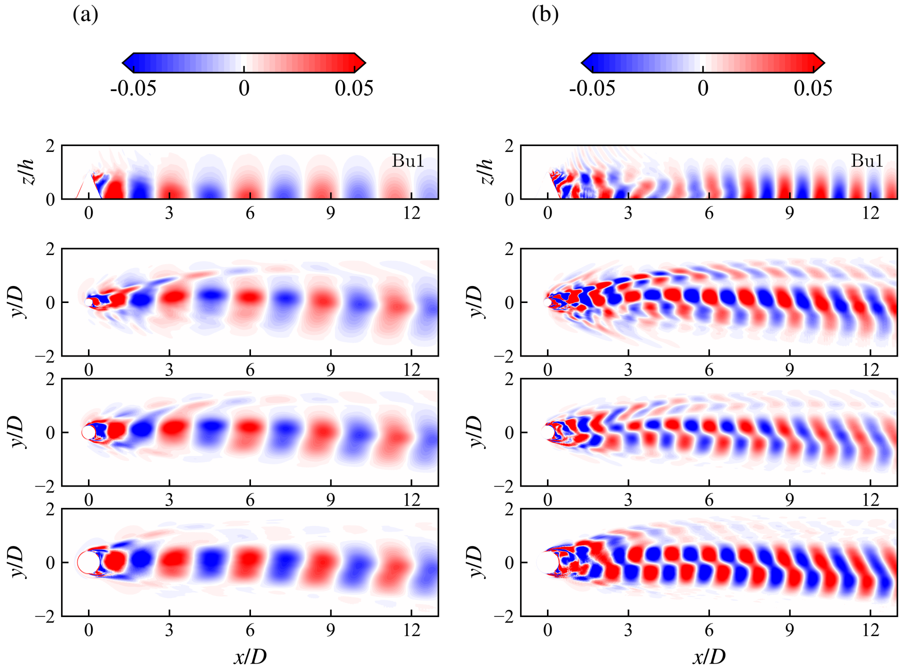

FIGURE 7. For case Bu1. Caption same as in figure 6.

that in the f_{VS} mode. A result of this reflection antisymmetry is that the eigenspectrum at the vertical plane (black dashed line in figure 4a) doesn't exhibit a peak at $2f_{\mathrm{VS}}$, unlike the spectra at horizontal planes. The antisymmetry implies a zero magnitude of the $2f_{\mathrm{VS}}$ mode at the centreline ($y = 0$), hence the top row in mode 4(b) does not imply any dynamical importance.

The imaginary parts of the eigenmodes are not shown, which are different from the real parts by a streamwise phase shift of $\pi/2$, and are therefore representing the same VS dynamics. The phase shift is essential for two standing-wave-like eigenmodes with the same streamwise wavelength (such as the real and imaginary parts of the f_{VS} mode) to accommodate a traveling-wave-like structure (such as the advecting VS motion) as noted by Rempfer & Fasel (1994).

For cases Bu25 and Bu1, the reflectional symmetry is broken by the Coriolis force and, unlike BuInf, the peak at $2f_{\mathrm{VS}}$ is observed in the eigenspectra at the vertical plane (black dashed lines). The rightward ($-y$) shift of the vortex wake is consistent with the direction of the Ekman veering of a bottom the unbalanced mean pressure gradient. This asymmetry can also be found in the SPOD modes in figures 6(c,d) and 7(a,b), where the cyclones (on the left side of the bulk of the wake, looking from above) are preferred and amplified, as compared to the anticyclones. However, in the vertical mode (first row in figure 6(c,d)), slanted structures are still statistically significant, even though figure 2(b) shows that, for case Bu25, some anticyclones have already become columnar. This suggests that the stratification in Bu25 is still dominating, and rotation has not been able to modify the spatial organisation of the structures. However, the presence of rotation significantly alters the structure inside the anticyclones, which will be analysed in section 5.

For case Bu1 (strong rotation), the global modes in figure 7(a-b) show excellent vertical alignment, agreeing with the shed 'columns' in figure 2(c). In the vertical plane (see the first row in figure 7a), both cyclonic and anticyclonic structures extend slightly higher than the obstacle peak, whereas the structures in cases Bu25 and BuInf are limited to below the obstacle peak, signifying that the obstacle's range of influence is vertically increased by increasing rotation. We note that those 'columns' are different from the typical Taylor column in rotating flow over obstacles. A Taylor column has an infinite height on the top of a finite object that generates it, whereas the columnar global mode in case Bu1 has a finite height. In figures 7(a,b) it can be seen that the parts of the global mode near the hill ($0 < x/D < 1$) are smaller and slanted, and they eventually become organised into tall 'columns' during their advection downstream as rotation is experienced, instead of being columnar at the generation.

4. Vortex centre tracking and advection velocity

The previous section on coherent structures was a macroscopic view that was enabled by the extraction of global SPOD modes. In this section, we will take a microscopic (at the level of individual vortices) view of the cyclonic (negative, note the Southern Hemisphere setting) and anticyclonic (positive) vortices. To do so, individual vortex centers will be identified and, by computation of statistics conditioned to them, various properties will be diagnosed on an ensemble-average basis: vortex advection velocity discussed in this section and, in section 5, the vorticity distribution inside the vortices and furthermore the stability of wake vortices as inferred by the application of linear-theory-based stability criteria of varying complexity.

The advection velocity in turbulent wakes past the near-wake stage can be taken to be close or equal to the freestream velocity U_∞, e.g., beyond $x = 6D$ in the study by VanDine *et al.* (2018) of non-rotating wakes at $Fr \geqslant O(1)$. Whether this constancy holds everywhere in the flow, and whether there is any asymmetric advection between the cyclonic and anticyclonic sides, requires clarification for geophysical wakes.

The present time-resolved database enables temporal tracking of the vortices to study their behaviour during the evolution. We apply a clustering method – mean shift to extract the vortex centres in horizontal snapshots, and then follow each identified centre in time. An example of identified vortex centres is illustrated in figure 8. Those centres are identified in one horizontal plane ($z/h = 0.50$) which is shown in the bottom row, and their projection onto the vertical central plane ($y = 0$) is shown in the top row. Symbols represent centres and are superposed on the vorticity field. To avoid the turbulent near-wake region where the wake vortices have not yet fully formed, the domain of vortex tracking starts at $x/D = 2$. The outflow region ($13 < x/D < 15$) is also not considered for vortex tracking, to avoid possible errors induced by the convective boundary condition. The implementation of the method is presented in detail in Appendix A.

An example of the trajectory of vortex centres is shown in figure 9 for case Bu1 at $z/h = 0.50$. Each trajectory is a sequence of streamwise locations of vortex centres x_c as a function of time t, and the local trajectory slope gives the local vortex advection velocity. It can be seen in figure 9 that the local slope is almost a constant throughout the downstream advection and the x_c-t trajectories are very close to straight lines.

In order to estimate the average vortex advection velocity (U_c) using all available data, a linear fit of each trajectory in the x_c-t diagram is performed to obtain the slope, and the advection velocity at a certain height (z/h) is the ensemble average over all trajectories at the same height. Since the advection velocity changes little as x increases, only trajectories that last longer than 50 snapshots (around one VS period) are considered to exclude the momentary tracking of small vortices other than the Kármán vortices. No significant difference is found in the results by changing this number to 25. In total, more than 80 trajectories are extracted for either positive or negative vortices in each case. The R^2 value of the linear regression

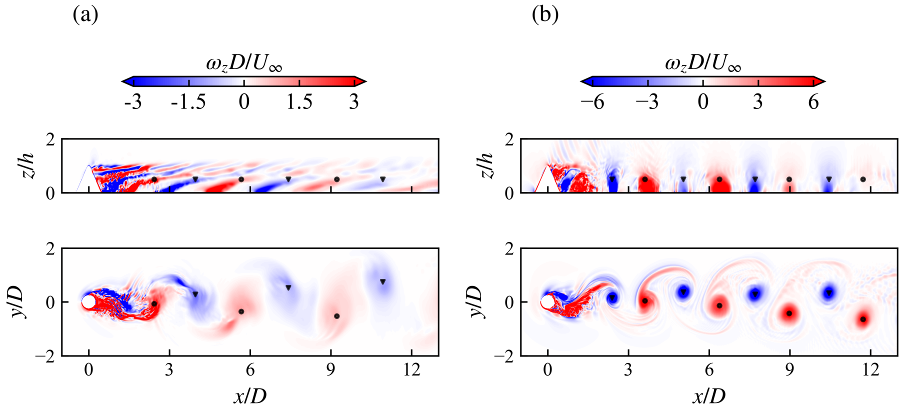

FIGURE 8. Visualisation of identified vortex centers, for cases (a) BuInf and (b) Bu1. Circles and triangles mark the centres of positive and negative vortices, respectively. Shown are the centres identified in a horizontal plane at $z/h = 0.50$ (bottom row) and their projection in the vertical central plane at $y = 0$ (top row).

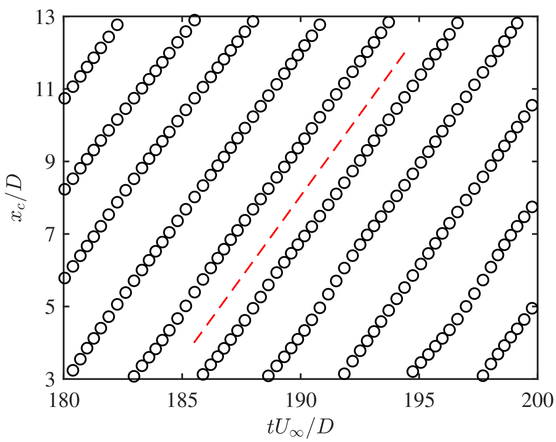

FIGURE 9. The x_c-t diagram of the trajectories of centers of positive vortices at $z/h = 0.50$ in case Bu1. Each black circle marks the instantaneous location x_c of a positive vortex centre, at a time t. The red dashed line has a non-dimensional slope of 0.9, corresponding to a vortex advection velocity of $0.9U_\infty$. For clarity, vortex centres are plotted every five snapshots.

exceeds 0.999 in all cases except for the positive vortices in Bu25, which has $R^2 > 0.99$, confirming the excellent constancy of the advection velocity throughout the investigated domain, $x/D = 3$ to $x/D = 13$. Table 2 lists the advection velocity for all three Burger numbers, for vertical planes $z/h = 0.12, 0.25, 0.50$.

For BuInf, U_c of positive and negative vortices are practically the same, as expected. Furthermore, U_c exhibits no significant variation from $z/h = 0.12$ to $z/h = 0.50$. In cases Bu25 and Bu1, anticyclones (positive vorticity) tend to move slower than cyclones (negative vortices), presumably due to their larger size (see figure 3), and this discrepancy is more pronounced at higher planes where vorticity is weaker. Among all the cases, Bu1 has the highest advection velocity as well as the smallest vortex sizes. Nevertheless, in all cases

Location	BuInf (+)	BuInf (−)	Bu25 (+)	Bu25 (−)	Bu1 (+)	Bu1 (−)
$z/h = 0.12$	0.877	0.880	0.894	0.888	0.902	0.910
$z/h = 0.25$	0.889	0.890	0.877	0.885	0.901	0.914
$z/h = 0.50$	0.868	0.872	0.868	0.889	0.891	0.916

TABLE 2. Vortex advection velocity (U_c) normalised by U_∞. Positive and negative vortices are denoted as '+' and '−', respectively. For all cases, the standard deviation for the advection velocity is less than $5 \times 10^{-3} U_\infty$.

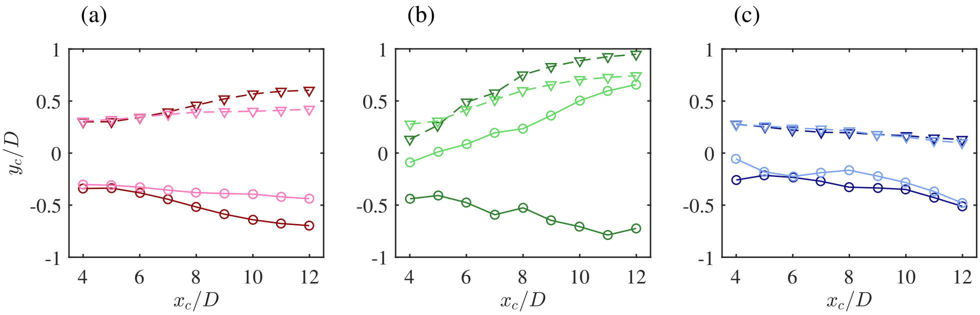

FIGURE 10. Averaged trajectories of identified vortex centres: (a) BuInf, (b) Bu25, and (c) Bu1. Solid lines with circles and dashed lines with triangles represent positive and negative vortices, respectively. Dark colors are for a lower plane at $z/h = 0.12$ and light colors for a higher plane at $z/h = 0.50$.

studied here, regardless of the sign of vorticity, location, and rotation Rossby number, the vortex advection velocities are very close, and can be well approximated by a single value, $U_c = 0.9U_\infty$. The near constancy of U_c is consistent with the observation of the global modes in section 3 that the tilting angles of the structures do not change as they evolve downstream. It is worth noting that the present results agree well with the measurement by Zhou & Antonia (1992) in laminar and turbulent cylinder wakes that the advection velocity is about $0.9U_\infty$.

The lateral motion of the vortices is also of physical and practical importance. Physically, the lateral movement of the vortices away from the centreline indicates the expansion of the wake and widening of the associated transport of mass, momentum, and any scalar fields in the flow. Practically, the mean locations of vortex centres and their variability are instructional to field observations as to where to place measurement stations and to experiments as to where to probe the flowfield. The simple choice of data sampling on a line at constant $y \neq 0$ is not ideal, as is shown by the curvature of the average path of vortex centres in figure 10. The average is performed locally in circles of radius $D/2$ whose successive centers ($x/D = 4, 5, ..., 12$) have an increment of D. Each symbol represents data from all vortex centres that fall in the range of $\pm D/2$ of the x-coordinate of the symbol. Solid and dashed lines are the averaged paths of positive and negative vortices, respectively. Results from two planes at $z/h = 0.12, 0.50$ are shown.

For case BuInf, the distance between positive and negative vortices slightly increases as they are advected downstream, as a result of diffusion of wake vorticity and the expansion of the wake. Taking that as a baseline, increasing rotation can either widen (Bu25, excluding positive vortices at $z/h = 0.50$ where dipoles are formed) or narrow (Bu1) the wake, indicating the nonlinear effect of rotation on wake width growth.

For case Bu1 (figure 10 c), the lateral locations of vortex centres are closest to the centreline, compared to the other two cases, and is consistent with the fact that both positive and negative vortices are most compact and smallest at the same z/h location in this case. Moreover, the entire wake characterised by vortex centres is slightly titled to the right ($-y$ direction), in agreement with the direction of the Ekman veering due to an unbalanced pressure gradient at the bottom boundary of rotating flows. In terms of the vertical alignment, the negative vortices are almost aligned perfectly in vertical throughout the downstream evolution, while positive vortices are not, indicating asymmetry between their properties which will be studied in detail in the next section.

For case Bu25, the wake is the widest on the left side since the paths of negative vortices have the most deviation from the centreline. It is worth mentioning that the light green solid line (at $z/h = 0.50$ in Bu25) is special. It represents the path of anticyclonic positive vortices that, statistically speaking, don't reside on the right side ($y < 0$) of the hill as other anticyclones but deviate to the left side ($y > 0$) instead. This is due to the influence of the stronger cyclonic negative vortices on the left side and the resultant formation of vortex dipoles with uneven vorticity that translate leftward, as shown by the visualisation in the middle row in figure 3(b). It is worth emphasizing that dipole formation and the resultant leftward deviation of the anticyclones is statistically significant. Generally, anticyclones are expected on the right side of the hill, but this is clearly not true for the particular case of Bu25 at $z/h = 0.50$.

5. Cyclones and anti-cyclones; marginal instability

In non-rotating unsteady wakes of bluff bodies with a symmetrical cross-section, there exists no statistical asymmetry in the mean between positive or negative vorticity as the reflectional symmetry is respected. As a result, in a classic cylinder wake or the present non-rotating case (case BuInf), the mean vertical vorticity is antisymmetric with respect to the centreline $y = 0$ (see figure 10d). However, the Coriolis force that accompanies system rotation breaks this reflectional symmetry. As the Coriolis frequency (f_c) is negative in this study, positive vortices ($\omega_z > 0$) are AVs and vice versa. The CVs and AVs present considerable differences in the rotating cases as illustrated by the visualisations of figure 3.

This section is arranged as follows: section 5.1 compares the probability distribution function (p.d.f.) of positive and negative ω_z in different cases and examines the systematic asymmetries and biases that rotation introduces to vorticity; section 5.2 utilises the vortex centres extracted in the previous section to obtain ensemble-averaged conditional statistics to characterize how vortex structure depends on rotation; 5.3 elaborates on the stability properties of AVs and their implication.

5.1. *Probability distribution of vorticity*

The p.d.f. of $|\omega_z|$ for positive vorticity (solid line) and negative vorticity (dashed line) are shown separately and on the planes $z/h = 0.12$ (figure 11a) and 0.50 (figure 11b). Each p.d.f. is normalised such that the area under each line is equal. For case BuInf, symmetry is achieved for vorticity of all magnitudes, as expected. Comparing cases Bu25 and Bu1, there is an increasing asymmetry between the p.d.f. of positive and negative vorticity, as the rotation strength is increased.

Consider the Bu1 case (blue lines). In plane $z/h = 0.12$ shown in figure 11(a), there is a local peak for cyclonic vorticity (negative ω_z) and one for anticyclonic vorticity (positive ω_z), both being slightly larger than the system rotation rate and close to $1.1|f_c|$. In plane $z/h = 0.50$ shown in figure 11(b), there is a local peak only for anticyclonic (positive) vorticity at $0.7|f_c|$.

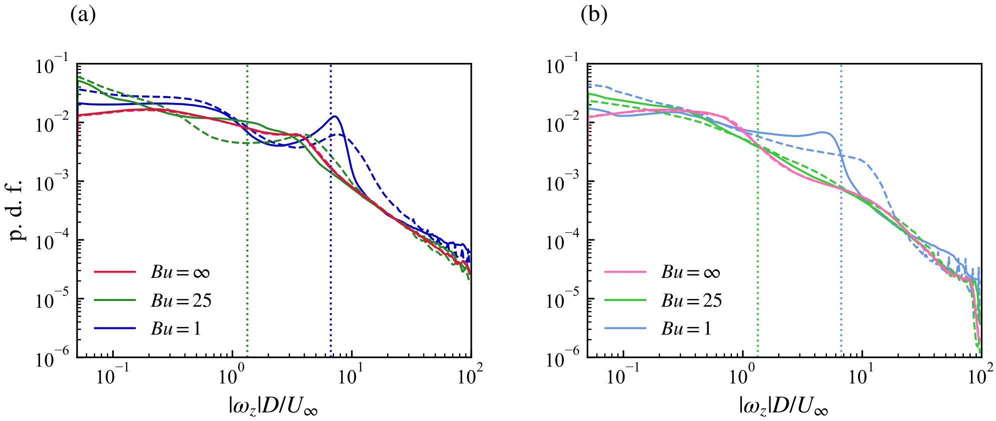

FIGURE 11. P.d.f. of $|\omega_z|$ at (a) $z/h = 0.12$, and (b) $z/h = 0.50$. Solid lines indicate positive vorticity (AVs), and dashed lines indicate negative vorticity (CVs). The vertical dotted lines represent the magnitude of the non-dimensional Coriolis frequency $|f_c|D/U_\infty = 1/Ro$, 4/3 for case Bu25 and 20/3 for case Bu1, respectively.

For case Bu25, the p.d.f. of cyclonic vorticity at $z/h = 0.12$ shown in figure 11(a) also has a peak above $|f_c|$ (with peak relative vorticity $3.1|f_c|$, which is significantly greater that in case Bu1). On the other hand, anticyclonic vorticity does not show any observable peak near $|f_c|$.

The local peaks in p.d.f.s are interpreted as the values that are more commonly found in the flow compared to their neighbours, instead of the most intense ones. In the next section, we will show the existence and persistence of intense anticyclones ($\omega_z > |f_c|$) in both Bu1 and Bu25 and discuss their stability.

5.2. *Vorticity conditioned to individually tracked vortices*

The vorticity distribution inside wake vortices is essential to the understanding of their kinematics, the idealisation and modelling of such vortical wakes, and the role of vortex stability. The previous section on vorticity p.d.f., while giving an overall statistical view of cyclonic/anticyclonic vorticity, does not reveal the properties of individual coherent wake vortices – the focus of this section. The identification of vortex centers in section 4 is leveraged to quantify the vorticity conditioned to the identified vortex centres and thus reveal the flow inside and around the vortices. As elaborated below, rotation significantly impacts the downstream evolution of the vortex-conditioned distribution of ω_z and, notably, the difference between AV and CV is larger for $Bu = 25$ than for $Bu = 1$.

Figure 12 shows profiles of the average of $\omega_z(\tilde{x})$, conditioned to instantaneous individual vortex centres. Here, $\tilde{x} = x - x_c$ with x_c denoting the streamwise location of the vortex center. Since wakes are spatially developing, the results are presented at various values of x_c to diagnose the downstream evolution of vortex-conditioned properties. Vortices with centres apart less than $2D$ are assumed to possess similar properties and grouped for a regional average. For example, the group located at $x_c/D = 4$ represents vortex centres that fall in the section of $3 < x/D < 5$ and so forth. Each vortex centre in the same group is shifted to $\tilde{x} = 0$ before the statistics are gathered. For each group, more than 2000 vortices are available for the ensemble average.

For case BuInf shown in figure 12(a,b), vorticity profiles are Gaussian-like except close to the edges. The peak magnitude decays and the width grows as a result of diffusion.

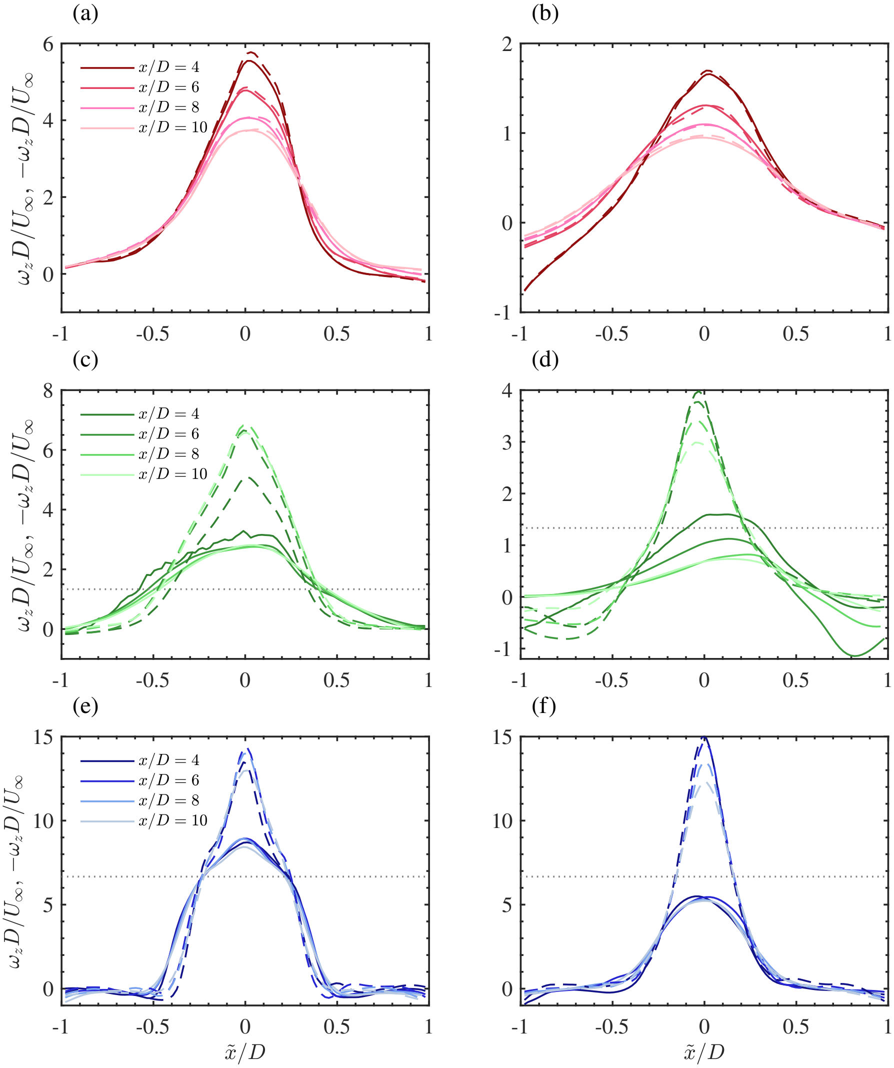

FIGURE 12. Conditionally averaged vorticity distribution around vortex centres, $\omega_z D/U_\infty$ for positive vortices (AVs, solid) and $-\omega_z D/U_\infty$ for negative vortices (CVs, dashed). (a,b) BuInf, (c,d) Bu25, and (e,f) Bu1. Horizontal planes shown are at $z/h = 0.12$ (a,c,e) in the left column and at $z/h = 0.50$ (b,d,f) in the right column. The horizontal dotted lines in (c,d,e,f) indicates the case-dependent absolute magnitude of the Coriolis frequency ($|f_c|$). In plots (c-f), the strongest CVs have peak magnitudes of $\omega_z/f_c = 5.1, 3.0, 2.2, 2.2$, and the strongest AVs have peaks $\omega_z/f_c = -2.4, -1.2, -1.3, -0.8$, respectively.

Otherwise, no significant change is present when x increases. In figure 12(a) at $z/h = 0.12$, the magnitude of ω_z near $x/D = \pm 1$ is close to zero – the asymptotic far-field condition for isolated vortices. However, in figure 12(b) at $z/h = 0.50$, the vorticity can change sign when $\tilde{x}/D$ varies between 0 and -1, becoming substantially negative for the group $x_c/D = 4$ but less so further downstream. A similar sign change is not observed when $\tilde{x}$ varies between 0 and 1. As seen in the middle and bottom rows of figure 3(a), wake vortices of both signs at $z/h = 0.50$ are more spatially diffuse than at $z/h = 0.12$ and are almost side-by-side in the region around $x/D = 4$, making possible the sign change of vorticity.

case	z/h	x_c/D	CV $-\omega_{z,p}D/U_\infty$	CV $-\omega_{z,p}/\lvert f_c\rvert$	CV $l_{0.05}/D$	AV $\omega_{z,p}D/U_\infty$	AV $\omega_{z,p}/\lvert f_c\rvert$	AV $l_{0.05}/D$
Bu25	0.12	4	5.1	3.8	1.09	3.2	2.4	1.64
		10	6.6	4.9	1.15	2.8	2.1	1.73
	0.50	4	4.0	3.0	1.15	1.6	1.2	1.23
		10	3.0	2.2	1.02	0.7	0.6	1.45
Bu1	0.12	4	13.5	2.0	0.74	8.7	1.3	0.88
		10	13.0	2.0	0.80	8.4	1.3	0.93
	0.50	4	15.0	2.3	0.75	5.5	0.8	0.80
		10	12.3	1.9	0.82	5.2	0.8	1.04

TABLE 3. Summary of the properties of cyclonic and anticyclonic vortices, at two horizontal planes $z/h = 0.12, 0.50$ and two streamwise locations of vortex centres $x_c/D = 4, 10$. The peak vertical vorticity $\omega_{z,p}$ is given in convective (U_∞/D) as well as rotation (f_c) units. Vortex sizes are characterised by $l_{0.05}$, which is the diameter at which the intensity of ω_z decays to $0.05\omega_{z,p}$.

For case Bu25 shown in figure 12(c,d), CVs and AVs are substantially different. CVs are stronger and more compact, while AVs are weaker and wider. The latter is likely because of the cyclo-geostrophic instability associated with the AVs upstream before the conditional statistics are gathered. In figure 12(c), the vorticity distribution for $x_c/D = 4$ displays short-wavelength wiggles and represents active instability of the AVs as can also be seen in the bottom row of figure 3(b). We emphasize that the short-wavelength wiggles are in a profile that is obtained by averaging over an ensemble of approximately 2000 members and are, thus, statistically significant. This is later confirmed in section 5.3 where the generalised Rayleigh discriminant on the left side of the aforementioned AVs is shown to lie beyond the stability limit.

Figure 12(d) shows differentiated behavior between CVs and AVs when the vortex edge is approached. The conditionally averaged vorticity in AVs (positive ω_z) tends to change sign toward the right end, while that around CVs (negative ω_z) changes sign toward the left end. This indicates a preferred configuration of vortex dipoles with a positive vortex on the left and a negative vortex on the right, as can be seen in the middle row of figure 3(b). At the same time, the dipoles are quite asymmetric; the positive ω_z AV is weaker and more spatially diffuse than its partner, suggesting that the weaker AVs are more susceptible to the induced motion of the CVs. It is also in case Bu25 that the asymmetry between CVs and AVs is most pronounced. In terms of the strength of the AVs, the vorticity magnitude in the vortex core exceeds $|f_c|$ at all streamwise locations in the plane at $z/h = 0.12$. Thus, the absolute vorticity stability criterion is not conclusive to the behavior of AVs since, contrary to that stability criterion, AVs with $|\omega_z| > f$ are found to advect in a stable manner.

Strong rotation favors the formation of coherent vortices. For case Bu1 shown in figure 12(e,f), both CVs and AVs are strongest in units of U_∞/D in all three cases. In the plane at $z/h = 0.12$, both CVs and AVs have magnitude greater than $|f_c|$ while only CVs exceed $|f_c|$ in the plane at $z/h = 0.50$. Moreover, both CVs and AVs undergo little change in terms of vorticity magnitude and distribution during their advection – a key difference from the other two Burger numbers. This is in agreement with the mean flow characteristics to be discussed in section 6 that the streamwise change in the momentum wake of Bu1 is slower than in the other two cases.

Table 3 summarises the properties of CVs and AVs, in terms of peak intensity and vortex size. The peak intensity $\omega_{z,p}$ is the maximum of ω_z of each curve in figure 12, and the vortex size $l_{0.05}$ is the horizontal distance within which the magnitude of ω_z is greater than $0.05\omega_{z,p}$. It can be seen that at the same spatial location, vortex intensity is generally higher in Bu1 in convective units (U_∞/D). Moreover, the sizes of both CVs and AVs are consistently smaller in case Bu1. In combination with greater peak vorticity, velocity gradients are much larger in vortices in case Bu1 than in Bu25. In terms of vorticity in units of f_c, Bu25 stands out with the largest magnitude of ω_z/f_c.

5.3. *Stability of anticyclones*

Vortex stability is an important question since it is related to the generation of turbulence and small-scale motions. Here, we assess the ability of various criteria in the literature to identify the stability characteristics of the advecting wake vortices of the present simulations. It will be shown that more recent criteria that account for stratification and viscous dissipation constitute a significant improvement over earlier attempts.

The study of the centrifugal (inertial) instability of swirling flows can be traced back to Rayleigh (1917) who showed that the flow could become unstable if the squared angular momentum decreases radially. The Rayleigh criterion is a necessary and sufficient condition for the instability of inviscid columnar vortices subject to three-dimensional axisymmetric perturbations (Drazin 2002). In a rotating frame, the Rayleigh criterion for inertial instability is equivalent to the existence of a region with a negative product of Coriolis frequency and absolute vorticity (Holton 1972),

$$f_c(\omega_z(r) + f_c) < 0, \tag{5.1}$$

or in terms of the local Rossby number (note f_c can take either sign),

$$Ro_L(r) = \frac{\omega_z(r)}{f_c} < -1. \tag{5.2}$$

The criterion for inertial instability, (5.1), is widely used and implies that anticyclones with vorticity magnitude exceeding $|f_c|$ are unlikely. However, it assumes a sheared parallel flow as the base state (Holton 1972). Kloosterziel & Van Heijst (1991) found in their experiment that CVs could be unstable too, contrary to (5.2) . With the inclusion of the centrifugal term, a generalised Rayleigh discriminant (Kloosterziel & Van Heijst 1991; Mutabazi *et al.* 1992) for centrifugal instability in rotating vortical flows was established as

$$\chi(r) = [\omega_z(r) + f_c][2\frac{u_\theta(r)}{r} + f_c] < 0, \tag{5.3}$$

where $\omega_z + f_c$ is interpreted as the absolute vorticity and $u_\theta + f_c r/2$ as the absolute velocity. It implies instability when the absolute velocity and absolute vorticity are of opposite signs. Equation (5.3) assumes a specific form (axisymmetric) of perturbations. Nevertheless, (5.3) is good enough in many circumstances since axisymmetric perturbations are, in general, more unstable than non-axisymmetric ones (Billant & Gallaire 2005).

The inclusion of stable stratification as well as finite vertical dissipation further complicates the determination of stability. With stratification that suppresses small wavenumbers and finite vertical dissipation that suppresses large wavenumbers, the range of unstable vertical wavenumbers is reduced and (5.3) overestimates the unstable region (Lazar *et al.* 2013*a*). To reduce the predicted unstable region, Lazar *et al.* (2013*a*) proposed a new criterion for the curve of marginally stable Burger number:

$$\sqrt{Bu_v} = \left(\frac{3}{8|a_0|}\right)^{3/2} \frac{1}{\sqrt{Ek}} \frac{(|2Ro_v + 1|)^{7/4}}{|Ro_v|}, \tag{5.4}$$

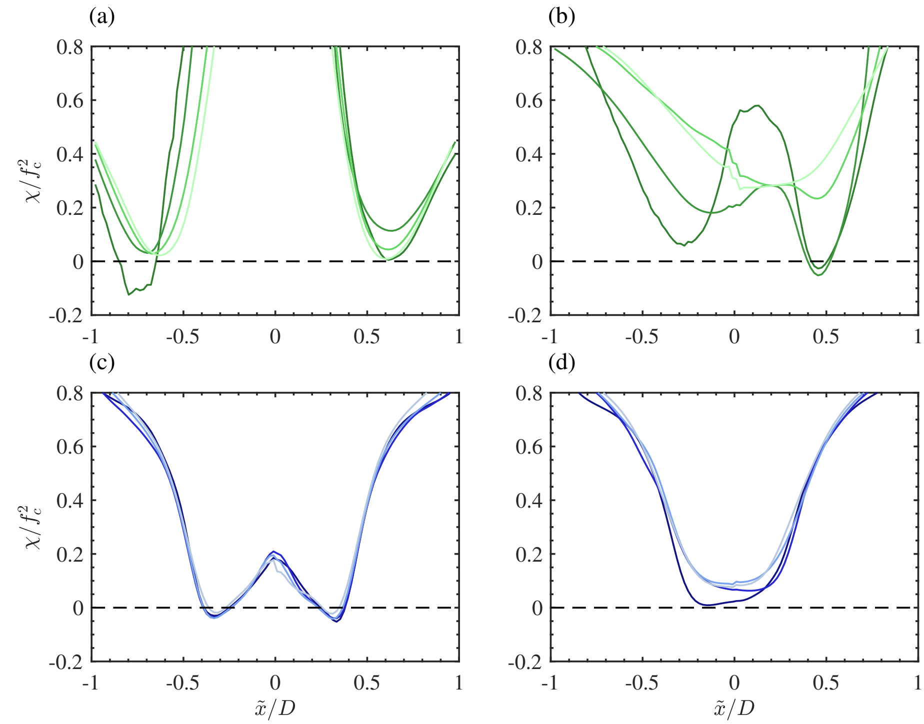

FIGURE 13. Conditionally averaged generalized Rayleigh discriminant χ/f_c^2 for AVs in cases Bu25 (a,b) and Bu1 (c,d). Horizontal planes shown are at $z/h = 0.12$ (a,c), and at $z/h = 0.50$ (b,d). Streamwise locations, $x/D = 4, 6, 8$ and 10 are shown in dark to light colors. The dashed line in each figure marks the stability criterion of $\chi = 0$.

where

$$Ro_{\rm v} = \frac{V_{\rm max}}{f_{\rm c} r_{\rm max}};\ Bu_{\rm v} = \left(\frac{Nh}{f_{\rm c} r_{\rm max}}\right)^2;\ Ek = \frac{\nu}{|f_{\rm c}|h^2} \tag{5.5}$$

are the vortex Rossby number, the vortex Burger number, and the vertical Ekman number. Here, $V_{\rm max}$ and $r_{\rm max}$ refer to the peak magnitude of the azimuthal velocity and its location, respectively. Positive and negative $Ro_{\rm v}$ represent cyclones and anticyclones, respectively. The constant $a_0 = -2.338$ is the first zero of the Airy function. In the parameter space of $Bu_{\rm v}$-$Ro_{\rm v}$, Eq. (5.4) at each constant Ek corresponds to a stability curve that separates regimes that are stable and unstable to axisymmetric perturbations.

Moreover, Yim *et al.* (2019) found that the most unstable azimuthal wavenumber of the centrifugal mode is not necessarily $m = 0$ (axisymmetric), but depends on $Bu_{\rm v}$ and will have an impact on the determination of stability. Accordingly, they suggested the use of the stability curve given as

$$\sqrt{Bu_{\rm v}} = \frac{0.23}{\sqrt{Ek}} \frac{(Ro_{\rm v} + 0.3)^2}{\sqrt{|Ro_{\rm v}|}}, \tag{5.6}$$

which considered the dependence of the most unstable azimuthal wavenumbers on $Bu_{\rm v}$. In this section, we will compare the absolute vorticity criterion (5.1), the generalised Rayleigh discriminant (5.3), as well as the new criteria (5.4) and (5.6), and assess their ability to predict the stability of the wake vortices in the simulations.

As was shown in figure 12(c,e), anticyclones at $z/h = 0.12$ are observed to possess a large

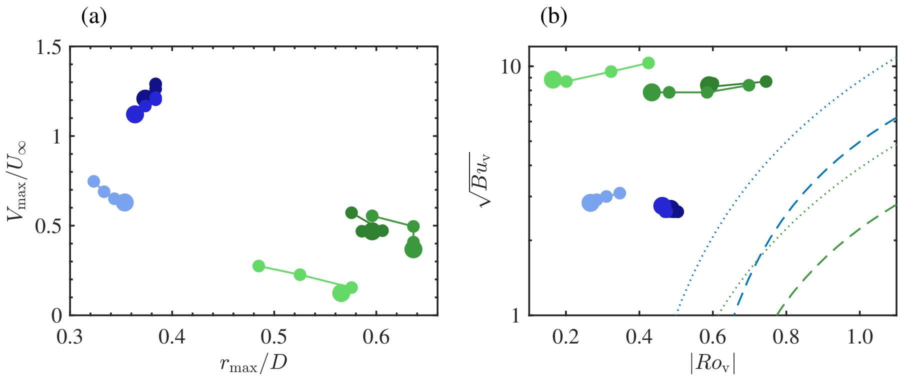

FIGURE 14. Vortex properties: (a) conditionally averaged maximum azimuthal velocity V_{max} and corresponding location r_{max} and (b) square-root of the vortex Burger number $\sqrt{Bu_v}$ and the vortex Rossby number Ro_v. Bu25 is shown in green and Bu1 in blue. Colors from dark to light indicate planes at $z/h = 0.12, 0.25, 0.50$. Each circle marks one of the locations from $x/D = 4, 6, 8, 10$. The circles are connected by lines following the order of x-locations and the last location ($x/D = 10$) is marked with the largest circle. In (b), dashed lines denote the stability curves (5.4) by Lazar *et al.* (2013*a*) and dotted lines (5.6) by Yim *et al.* (2019) for cases Bu1 (blue) and Bu25 (green). The Ekman numbers are $Ek = |Ro|/Re_D(D/h)^2 = 8.33 \times 10^{-4}$ and 1.67×10^{-4} for cases Bu25 and Bu1, respectively. The left side of the neutral stability curves is stable.

region with $|\omega_z| > |f_c|$, although they advect as stable vortices for a significant range of downstream evolution distance. Hence, the absolute vorticity condition (5.1) is not sufficient for instability.

Figure 13 shows the conditionally averaged generalized Rayleigh discriminant $\chi(\tilde{x})$ in (5.3) as a function of streamwise distance from the vortex centre. It can be seen that the unstable region is reduced significantly compared to (5.1). In case Bu25 and at $z/h = 0.12$ (figure 13a), at roughly $x/D = 4$ (the darkest green line), there is a small region, located near the left edges of the AVs, that is found to be unstable, but otherwise, all regions have at least marginally stable χ. Furthermore, the vortices tend to evolve to a more stable state. For Bu1, the AVs in the $z/h = 0.50$ plane (figure 13b) have stable discriminant χ, while the peripheries of the AVs in the plane $z/h = 0.12$ have marginally unstable χ which does not experience noticeable change during the advection. The statistics of χ of the AVs in the plane at $z/h = 0.25$ are similar to those at $z/h = 0.12$ and are not shown. Consistent with the instantaneous snapshots in figure 3 and the statistics in figure 12, AV instability is only observed for Bu25 at $z/h = 0.12$, and is captured properly by the generalized Rayleigh discriminant (5.3). On the other hand, in case Bu1 at $z/h = 0.12$ (figure 13c) where the discriminant is marginally unstable at the periphery of the vortices, no actual change to the vorticity profile of the AVs is observed (see figure 12e). Hence, a sufficient condition for stability requires other considerations, e.g., stratification and dissipation (Lazar *et al.* 2013*a*; Yim *et al.* 2019).

Prior to applying (5.4) and (5.6), the vortex sizes and shapes in terms of V_{max} and r_{max} are required. The radial direction is substituted by the streamwise (x) direction and the azimuthal velocity component by the spanwise velocity (v). The peak velocity V_{max} is defined as the maximum azimuthal (herein transverse) velocity and the corresponding peak location r_{max} is interpreted as vortex radius.

Figure 14(a) shows V_{max} and r_{max} for Bu 25 and Bu1 at various streamwise locations. It can be seen that for both Bu1 and Bu25, the vortex radii agree reasonably well with the radial location of the least stable χ (figure 13), consistent with theoretical analysis and experimental observation that the edges of vortices are the least stable regions (Kloosterziel & Van Heijst 1991; Carnevale *et al.* 1997; Lazar *et al.* 2013*a*; Yim *et al.* 2016). Moreover, AVs in Bu25 have a much larger radii as well as variability during the evolution, compared to Bu1. The AVs in Bu1, which have greater $V_{\max}$ (over twice stronger than Bu25) and smaller vortex radii, have the largest average vorticity.

Figure 14(b) shows the evolution of AVs, on average, in the Bu_v-Ro_v parameter space. The AVs in both Bu25 and Bu1 are characterised by vortex Rossby numbers of $O(0.5)$. The stability curves (5.4) and (5.6) are also plotted for cases Bu1 and Bu25. The left side of a stability curve is the stable region, and vice versa. It can be seen that all AVs in both cases fall on the stable side, and they all tend to evolve to a more stable state (lower $|Ro_v|$ and further away from the stability limit). The stability results are in agreement with our observation that there is no apparent sign of instability of AVs except for at $z/h = 0.12$ in Bu25, where AVs are still not independently distinguishable from the turbulent near wake. The more conservative determination of cyclo-geostrophic instability in the present wakes utilising (5.4) and (5.6) as compared to (5.3) also confirms the point of view in Lazar *et al.* (2013*a*); Yim *et al.* (2019) that in real geophysical environments, stratification and vertical dissipation will further shrink the range of unstable vertical wavenumbers from the low- and high-wavenumber end, respectively, and lead to a greater range of stability.

6. Mean momentum wake

Stratified wakes in engineering applications, e.g. submersibles in the ocean, typically have $Fr \geqslant O(1)$ and negligible rotation effects. Momentum wakes in these applications are known to have very different properties compared to their unstratified counterparts, e.g. a buoyancy-induced slowdown in the decay of mean momentum deficit in the so-called non-equilibrium stage (Spedding 1997; Brucker & Sarkar 2010; Diamessis *et al.* 2011; de Stadler & Sarkar 2012). Stratified wakes, which have been extensively studied for the sphere, have been investigated recently for a blunt body – a disk (Chongsiripinyo & Sarkar 2020) and a slender body – a 6:1 prolate spheroid (Ortiz-Tarin *et al.* 2023). In rotating stratified wakes studied here, with the presence of coherent wake vortices and cyclo-geostrophic balance, the mean flow is further influenced as will be elaborated below. Examination of the momentum deficit profiles of this section shows enhanced persistence of the wake that has implications in oceanography and meteorology. For example, even at $x = 12D$, the wake deficit behind the near-bottom portion of the hill/seamount is as large as $0.4U_\infty$. Thus, absent other interacting flow features, bottom roughness or other bathymetry, the wake of a steep 10 km base-diameter hill would be preserved for 120 km. Also, a steep 3D topographic feature would lead to a bottom flow (outside the viscous boundary layer) with significant shear, for instance, a difference over obstacle height of 0.2 to 0.4 times U_∞.

Figure 15(a) shows profiles of mean velocity deficit, $U_d(y) = U_\infty - \langle U\rangle(y)$, at various streamwise locations in the plane $z/h = 0.12$ (a,c,e) and figure 15(b) shows the streamwise evolution of the centerline deficit velocity ($U_0 = U_d(y = 0)$) along various heights (b,d,f). The symbol $\langle\cdot\rangle$ denotes the time average over the duration of data storage listed in table 1.

The non-rotating case BuInf (figure 15a) exhibits $U_d(y)$ profiles that are laterally symmetric. The centerline velocity deficit ($U_0(x)$ in figure 15b) initially decreases after the recirculation bubble but then increases again. This is consistent with the expansion and shrinking of the $\langle\omega_z\rangle(y)$ width in figure 3(d). In low-Re two-dimensional cylinder wakes, $U_0(x)$ has a similar non-monotonic behaviour (Kumar & Mittal 2012) and the vorticity profile width also has a non-monotone variation (Barkley 2006). On the other hand, after the recirculation zone, $U_0(x)$ exhibits monotone decay in three-dimensional unstratified wakes.

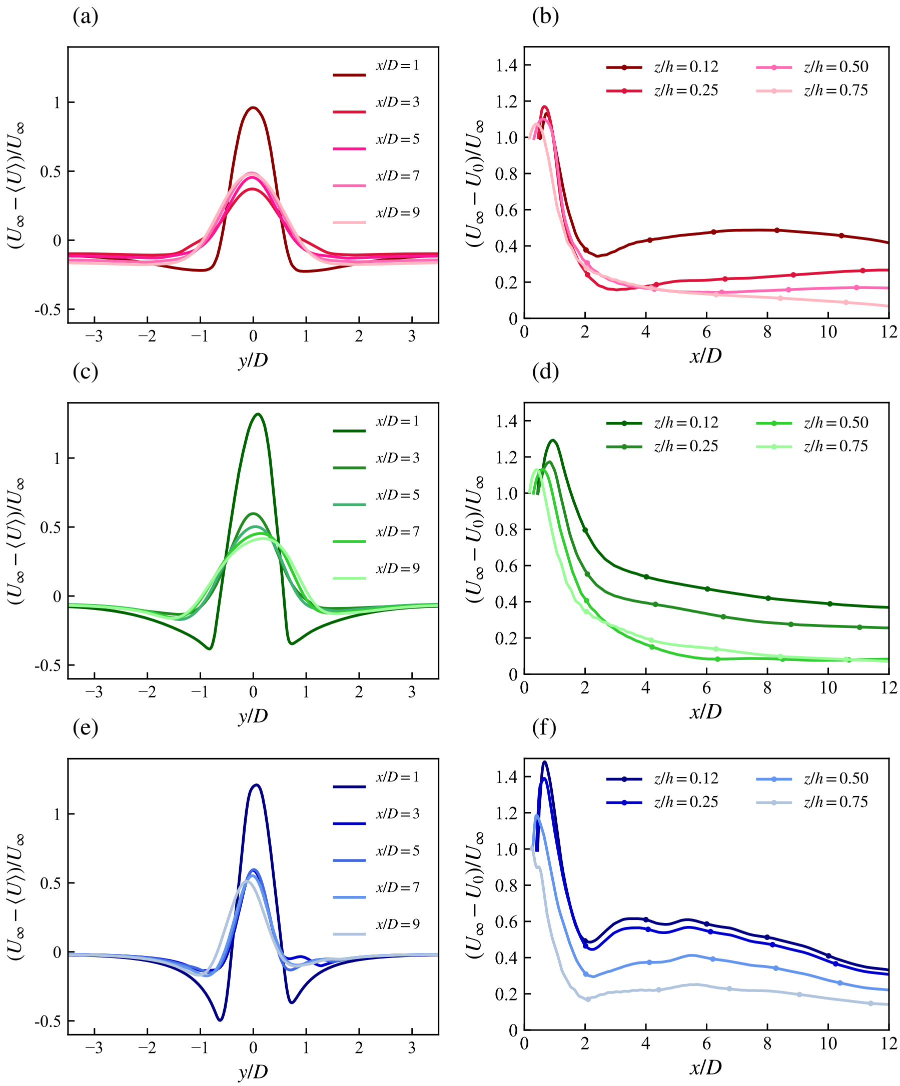

FIGURE 15. Time-averaged velocity deficit in the wake for cases BuInf (top row), Bu25 (middle row) and Bu1 (bottom row). Left column (a,c,e) shows transverse profiles of velocity deficit at $z/h = 0.12$ and various $x/D = 1, 3, 5, 7, 9$ (from dark to light). Right column (b, d, f) shows the streamwise evolution of the centerline ($y = 0$) deficit at various elevations, $z/h = 0.12, 0.25, 0.50, 0.75$ (from dark to light).

This similarity of the mean deficit between two-dimensional wakes and non-rotating stratified wakes, where the third dimension is confined by buoyancy, is intriguing.

In the rotating cases Bu25 and Bu1, the lateral symmetry of the mean wake is lost as shown in figure 15(c,e). Rotation at $Ro = 0.75$ (Bu25) leads to the instability and diffusivity of AVs (commented on previously) and results in a wider wake compared to BuInf. However, stronger rotation at $Ro = 0.15$ (Bu1) creates tall shedding 'columns' that are compact and almost 'frozen' during evolution, leading to a narrower wake instead. Comparing the centreline deficit (figure 15), case Bu1 sustains the highest overall velocity deficit (roughly above $0.2U_\infty$ at all planes) compared to the other two cases, presumably due to the lower diffusivity and higher degree of vortex coherence. In the lower portion of the hill ($z/h = 0.12$) all three cases exhibit significant $U_0 \approx 0.4U_\infty$ showing persistence of the near-bottom wake in stratified flow, independent of rotation.

7. Concluding remarks

Wake vortices in stratified flows past an isolated bottom obstacle are studied via LES, at moderately high Reynolds number ($Re_D = 10\,000$) and moderately strong stratification ($Fr = 0.15$). The rotation Rossby number is varied to include cases representing non-rotating ($Ro = \infty$), submesoscale ($Ro = 0.75$), and mesoscale ($Ro = 0.15$) wakes, resulting in Burger numbers of $\infty, 25, 1$. In all three cases studied, the wakes present Q2D Kármán vortex shedding in horizontal planes in the core of the wakes, which is a distinct feature of strongly stratified wakes.

The statistical spatio-temporal coherence of the Kármán vortices is analysed with SPOD. It is found that, at the present stratification ($Fr = 0.15$) and regardless of the rotation strength, the shedding frequency is a global constant in each case that is independent of height from $z/h = 0.12$ to $z/h = 0.75$, which is the core of the wake away from the bottom boundary layer and the region influenced by the lee waves near the top of the hill. This implies that, at the present stratification, VS frequency can stay coupled vertically, instead of varying as a function of the local (z-dependent) diameter. The vertical coupling occurs even when rotation is weak compared to stratification, a result that is inconsistent with the result of Perfect *et al.* (2018) that vortices are vertically decoupled when $Bu^* > 12$ or, converting to our definition, $Bu > 3$. However, it is quite possible that, when stratification is further increased, the VS frequency could vary with elevation.

Boyer *et al.* (1987) measured the VS frequency in a single plane as part of their experimental study of the wake behind a conical obstacle in linearly stratified rotating flows. The frequency showed little variation in their parametric study that spanned $0.08 < Fr < 0.28, 0.06 < Ro < 0.4$, and three Reynolds numbers $Re_D = 380, 760, 1140$. The lack of rotational influence on the VS frequency in the present work, which is at an order of magnitude larger Re_D, agrees with Boyer *et al.* (1987).

Another implication of a global shedding frequency is that the spatial assemblies of SPOD eigenmodes shown in figures 6-7 are 3D global modes that optimally represent the vertical enstrophy of the flow. In the non-rotating case BuInf (figure 6(a,b)), VS structures are slanted (yet three-dimensionally coherent) 'tongues' that tilt to the direction of the flow and form a very shallow angle (steeper near the bottom and shallower above, but at 4° on average) with the horizontal. The streamwise inclination of the structures appears to be preserved during the downstream evolution and was explained by a constant advection velocity of vortices at different heights. Rotation is found to have an influence on the vertical complexity of the global modes, as the shape of the global modes change from slanted structures to vertical 'columns' as the rotation increases. However, the value of VS frequency was almost constant (only a mild change of St_{VS} over 0.25-0.27) for the different Rossby numbers investigated.

It is worth noting that despite the turbulence in the near wake, the flow exhibits overall low-rank behaviour globally owing to the emergence of coherent structures. The low-rankness is two-fold. First, the enstrophy spectra in figure 4 show dominant spikes at the VS shedding frequency and its harmonics. Second, the gaps between eigenspectra shown in figure 5 indicate increasingly lower enstrophy in higher-order modes at each frequency. That being said, the large scales of the flow can be well described by a finite set of harmonic modes. This simplicity might encourage future reduced-order modelling of the coherent motion of wake eddies in similar parameter regimes.

Besides the macroscopic view of the vortex structures as global modes and how they vary at different Ro, a detailed examination of the profiles and evolution of the vortices is conducted. A novel way of tracking vortices automatically in time-resolved snapshots is applied on the LES database. Vortex centres (centres of regions of strong ω_z) are extracted with the mean shift algorithm (Fukunaga & Hostetler 1975; Comaniciu & Meer 2002) in each snapshot on 2D horizontal planes. Then the history of vortex centres in time is compiled into graphs that represent evolution trajectories. Finally, conditional statistics are gathered and ensemble averaged on the paths of vortex evolution.

The vortex advection velocity, extracted from the time history of vortex centres, is found to be near $0.9U_\infty$ in all three Bu cases, which is quite constant vertically as well. The vertically constant advection velocity explains the preserved vertical orientation of vortex structures during evolution, in all cases. However, it is slightly different for cyclones and anticyclones in the rotating cases presumably due to their size difference.

In geophysical flows, individual vortices are greatly influenced by background rotation. The adjustment of ω_z to rotation as well as the cyclo-geostrophic instability of AVs, are analysed by computing the statistics conditioned to identified vortex centres. The conditionally averaged vorticity profiles reveal that dynamical processes during the downstream advection of the vortices depend substantially on rotation. In case BuInf, the distribution of ω_z is Gaussian-like, with the diffusion-induced downstream increase of size and decrease of peak vorticity being the major feature. In case Bu25, the asymmetry between CVs and AVs is most significant among all three cases, and the magnitude of $|\omega_z/f_c|$ is also higher than in the other rotating case (Bu1). In case Bu1, both the CVs and AVs achieve the greatest magnitude of vorticity in convective units, i.e., $|\omega_z D/U_\infty|$, due to the enhancement by rotation. Also, both AVs and CVs experience little change during their evolution, implying that the vortices in case Bu1 are already in a balanced state.

Relatively strong anticyclones (e.g., core relative vorticity $\omega_z/f_c \approxeq -1.3, -2.4$ for Bu1 and Bu25 respectively, at $z/h = 0.12$) are found stable for a considerable distance of advection (figure 12(c,e)). They would be unstable according to the absolute vorticity criterion (5.1), which implies inertial instability when anticyclonic vorticity is stronger than the Coriolis frequency ($\omega_z/f_c < -1$). The inclusion of centrifugal contribution is shown as necessary by examining the generalised Rayleigh criterion (Kloosterziel & Van Heijst 1991; Mutabazi *et al.* 1992), which predicts overall stability in the bulk of the AVs and marginal instabilities at the edges, in agreement with observations of stable AVs in the wake. Two new recently proposed criteria (Lazar *et al.* 2013*a*; Yim *et al.* 2019) considering the effects of stratification and vertical dissipation are also tested. Both criteria are in terms of the marginal stability curves given by (5.4) and (5.6) in the parameter space of Bu_v-Ro_v, where Bu_v and Ro_v are the local (vortex) Burger and Rossby numbers specific to the local vorticity profile. Further restricting the range of unstable vertical wavenumbers by including stratification and dissipation, the criteria (5.4) and (5.6) both determine the AVs in the present work as stable as shown in figure 14(b). The only marginally unstable wake vortices are found in case Bu25 at $z/h = 0.12$ (see $x/D = 2$-3 in the last row of figure 3b and figure 13a), where the left side of the eddies at downstream location $x/D \sim 4$ is unstable. Further downstream, the region of instability disappears.

Statistically, when the AVs evolve downstream, they tend to approach a more stable state characterised by a larger (more stable) χ (figure 13), a smaller vortex Rossby number Ro_v (figure 14a), and a greater distance from the marginal stability curve (figure 14b). It is noted that in the present wakes, AVs are observed to be stable in the streamwise extent of vortex tracking (after $x/D \sim 3$). Since both Rossby numbers studied (0.75 and 0.15) are smaller than order unity, a Rossby radius of deformation defined as $U_\infty/|f_c| = RoD$ which can be regarded as a distance required for cyclo-geostrophic adjustment, will be smaller than $3D$ downstream. It is possible that at larger Rossby numbers, more unstable AVs will be observed further than $x/D > 3$ where the vortex tracking and stability determination are not obscured by near-wake turbulence.

In terms of future work, it would be useful to study wake vortices in other parameter regimes with non-hydrostatic simulations. Cases at lower Fr and a wide range of Ro are of particular interest with respect to the variation of vortex shedding frequency. Submesoscale instabilities at high Ro and high Re are possible and need investigation. Near-wake turbulence and mixing are also important follow-up topics in the context of the broader theme of ocean turbulence and mixing. Theoretical global stability analyses of stratified wakes would also provide a more complete picture.

Funding. This work is supported by ONR grant N00014-22-1-2024.

Declaration of interest. The authors report no conflict of interest.

Author ORCIDs.
J. Liu https://orcid.org/0000-0003-4133-0930
P. Puthan https://orcid.org/0000-0003-2690-0560
S. Sarkar https://orcid.org/0000-0002-9006-3173

Appendix A. A vortex tracking method for time-resolved databases

Mean shift (Fukunaga & Hostetler 1975; Comaniciu & Meer 2002) is a widely used method for pattern recognition in data analysis. It identifies centroids of condensed data points and then segments the data according to the centroids they belong to. This method can be applied to physical science as a means of data clustering, where some shared properties are expected for data points in the same cluster. It is unsupervised in the sense that either the number of clusters is required or the shape of clusters is prescribed. The basic idea is to move a provisional centroid iteratively toward the local maximum of the population density, hence it is also called a density-based method.

Similar to the implementation in Gong (2015), the mean shift algorithm is summarised as follows:

Step 1. Randomly select an initial seed for the i-th centroid $V_i^{(0)}$ from all unclustered points, or use the centroid computed in the n-th iteration $V_i^{(n)}$.

Step 2. Compute the centre of geometry (the so-called mean, denoted as $V_i^{(n+1)}$) of the data points that fall in the open ball $\mathcal{B}(V_i^{(n)}, r_{\mathrm{BW}})$, where $V_i^{(n)}$ is the ball centre and r_{BW} is the radius.

Step 3. If the Euclidean distance $|V_i^{(n+1)} - V_i^{(n)}|$ between $V_i^{(n+1)}$ and $V_i^{(n)}$ is below the tolerance, accept $V_i^{(n+1)}$ as V_i. Otherwise, use $V_i^{(n+1)}$ as the new seed to restart *Step 1*.

Step 4. Compare the Euclidean distance of the centroid V_i, to all existing centroids $\{V_l\}_{l=1}^{i-1}$ from previous iterations, and if $\exists j$, s.t. $|V_i - V_j| < 1/2r_{\mathrm{BW}}(0 < j < i)$, merge V_i and V_j and label their mean as V_j. Run through the distance check in *Step 4* for V_j in the set $\{V_l\}_{l=1,l\neq j}^{i-1}$.

Step 5. Check if there are unvisited points. If yes, start over from *Step 1*; otherwise, terminate.

The core steps 2-3 are illustrated in figure 16, where the shift of the mean is indicated by an arrow. Based on the mean shift algorithm, the vortex centre identification and tracking process utilised in this paper is summarised as follows:

(1) Mask the vorticity field. Convert each 2D vorticity field at a certain height $\omega_z(x, y, t; z)$ into a binary field, with ones denoting points with $\omega_z > \alpha$ (if identifying positive vortex centres) or $\omega_z < -\alpha$ (if identifying negative vortex centres), and zeros denoting the rest. Here a positive constant $\alpha(z)$ is a threshold individually selected for each horizontal plane

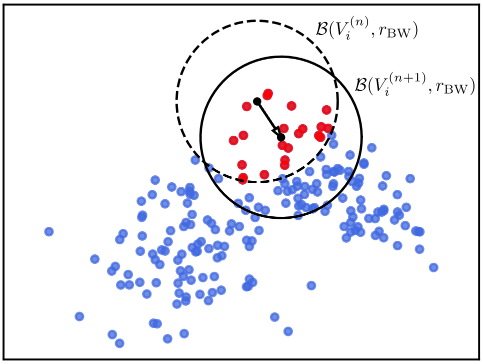

FIGURE 16. Illustration of the principle of the mean shift algorithm. Data points are randomized and are for illustration purposes only. The symbol $\mathcal{B}(V_i^{(n)}, r_{\rm BW})$ denotes an open ball with its centre at $V_i^{(n)}$ and radius $r_{\rm BW}$, where $V_i^{(n)}$ is the n-th iteration of the i-th centroid, and $r_{\rm BW}$ is the half bandwidth. The centroid $V_i^{(n+1)}$ represents the geometric centre of all data points enclosed by the ball $\mathcal{B}(V_i^{(n)}, r_{\rm BW})$ shown in red. The arrow denotes the shift of the mean (centroid).

to disconnect vortices from each other. We note that the hill wake is inhomogeneous in all three spatial directions and a global constant α does not apply.

(2) Apply the mean-shift algorithm to identify (usually a handful of in our flow) centres in each snapshot. Use $V_{i,k}$ to label the i-th vortex centre ($1 \leqslant i \leqslant n_{\rm max}$, where $n_{\rm max}$ is the maximum number of centres allowed) in the k-th snapshot ($1 \leqslant k \leqslant N_t$). The half bandwidth $r_{\rm BW}(z)$ needs to be selected as a parameter individually for each plane, and is chosen to be roughly 1.5 times the radius of a vortex, which is also smaller than the separation between two same-sign vortices.

(3) Construct the graphs of vortex centre trajectories, with each centre $V_{i,k}$ ($1 \leqslant i \leqslant n_{\rm max}, 1 \leqslant k \leqslant N_t$) being a node. Only the connections (edges) between two nodes from two consecutive snapshots are considered, with the connection weights being the Euclidean distance between these two nodes $\Delta x_c = |x_c(V_{i,k}) - x_c(V_{j,k+1})|$, where x_c stands for the streamwise location of the centre. Two nodes are considered to belong to the history of the same vortex (and hence belong to the same subgraph) if $\Delta x_c < 1.5 U_\infty \Delta t$, where Δt is the time elapsed between these two snapshots. All connection weights that don't satisfy this restriction will be set to zero. The choice of the separation distance $1.5 U_\infty \Delta t$ is meant to be inclusive since it is unlikely for the vortex centres to travel much faster than the background flow. On the other hand, this distance is small enough compared to the distance between two distinct vortices. After doing so, it is almost ensured that each centre will only have one forward and one backward connection in time. Each self-connected subgraph represents a vortex evolution trajectory within the domain.

It is noted that the identification and tracking method described above has limitations, such as requiring user input of a constant radius of searching, which is *a priori* knowledge about the physical system and was chosen to be around 1.5 times the radius of Kármán vortices in each plane. Hence, this method may not work in more complicated situations such as in flows that have a wide range of scales of vortices, or in processes involving vortex merging or splitting where two same-sign vortices can get too close. But for the present vortex wakes and other similar vortical flows where the organisation and evolution of vortices is clear, the computer-aided identification and tracking scheme is shown to be useful and easy to implement. Owing to the continuing advancement of computer power and experimental techniques, time-resolved databases are becoming more available, where our snapshot-based tracking method may facilitate the analysis of coherent structures in other types of flows and will therefore be of broader interest.

REFERENCES

Arbic, B. K. & Scott, R. B. 2008 On quadratic bottom drag, geostrophic turbulence, and oceanic mesoscale eddies. *Journal of Physical Oceanography* **38** (1), 84–103.

Bakewell Jr, H. P. & Lumley, J. L. 1967 Viscous sublayer and adjacent wall region in turbulent pipe flow. *The Physics of Fluids* **10** (9), 1880–1889.

Balaras, E. 2004 Modeling complex boundaries using an external force field on fixed cartesian grids in large-eddy simulations. *Computers & Fluids* **33** (3), 375–404.

Barkley, D. 2006 Linear analysis of the cylinder wake mean flow. *EPL (Europhysics Letters)* **75** (5), 750.

Barkley, D. & Henderson, R. D. 1996 Three-dimensional Floquet stability analysis of the wake of a circular cylinder. *Journal of Fluid Mechanics* **322**, 215–241.

Billant, P. & Gallaire, F. 2005 Generalized Rayleigh criterion for non-axisymmetric centrifugal instabilities. *Journal of Fluid Mechanics* **542**, 365–379.

Boyer, D., Davies, P., Holland, W., Biolley, F. & Honji, H. 1987 Stratified rotating flow over and around isolated three-dimensional topography. *Philosophical Transactions of the Royal Society of London. Series A, Mathematical and Physical Sciences* **322** (1564), 213–241.

Brucker, K. A. & Sarkar, S. 2010 A comparative study of self-propelled and towed wakes in a stratified fluid. *Journal of Fluid Mechanics* **652**, 373–404.

Carnevale, G., Briscolin, M., Kloosterziel, R. & Vallis, G. 1997 Three-dimensionally perturbed vortex tubes in a rotating flow. *Journal of Fluid Mechanics* **341**, 127–163.

Castro, I., Snyder, W. & Marsh, G. 1983 Stratified flow over three-dimensional ridges. *Journal of Fluid Mechanics* **135**, 261–282.

Chang, M.-H., Jan, S., Liu, C.-L., Cheng, Y.-H. & Mensah, V. 2019 Observations of island wakes at high Rossby numbers: Evolution of submesoscale vortices and free shear layers. *Journal of Physical Oceanography* **49** (11), 2997–3016.

Chongsiripinyo, K., Pal, A. & Sarkar, S. 2017 On the vortex dynamics of flow past a sphere at $Re = 3700$ in a uniformly stratified fluid. *Physics of Fluids* **29** (2), 020704.

Chongsiripinyo, K. & Sarkar, S. 2020 Decay of turbulent wakes behind a disk in homogeneous and stratified fluids. *Journal of Fluid Mechanics* **885**, A31.

Comaniciu, D. & Meer, P. 2002 Mean shift: A robust approach toward feature space analysis. *IEEE Transactions on Pattern Analysis and Machine Intelligence* **24** (5), 603–619.

Diamessis, P. J., Spedding, G. R. & Domaradzki, J. A. 2011 Similarity scaling and vorticity structure in high-Reynolds-number stably stratified turbulent wakes. *Journal of Fluid Mechanics* **671**, 52–95.

Dong, C., McWilliams, J. C. & Shchepetkin, A. F. 2007 Island wakes in deep water. *Journal of Physical Oceanography* **37** (4), 962–981.

Drazin, P. G. 2002 *Introduction to Hydrodynamic Stability*, , vol. 32. Cambridge university press.

Fey, U., König, M. & Eckelmann, H. 1998 A new Strouhal-Reynolds-number relationship for the circular cylinder in the range $47 < Re < 2 \times 10^5$. *Physics of Fluids* **10** (7), 1547–1549.

Fukunaga, K. & Hostetler, L. 1975 The estimation of the gradient of a density function, with applications in pattern recognition. *IEEE Transactions on Information Theory* **21** (1), 32–40.

Garcia-Villalba, M., Li, N., Rodi, W. & Leschziner, M. 2009 Large-eddy simulation of separated flow over a three-dimensional axisymmetric hill. *Journal of Fluid Mechanics* **627**, 55–96.

Gong, H. 2015 Interactive shadow removal. PhD thesis, University of Bath.

Haidvogel, D. B. & Beckmann, A. 1999 *Numerical Ocean Circulation Modeling*. World Scientific.

Holmes, P., Lumley, J. L., Berkooz, G. & Rowley, C. W. 2012 *Turbulence, Coherent Structures, Dynamical Systems and Symmetry*, 2nd edn. Cambridge university press.

Holton, J. R. 1972 *An Introduction to Dynamic Meteorology*. Academic Press.

Horvath, A., Bresky, W., Daniels, J., Vogelzang, J., Stoffelen, A., Carr, J. L., Wu, D. L., Seethala, C., Günther, T. & Buehler, S. A. 2020 Evolution of an atmospheric Kármán vortex street from high-resolution satellite winds: Guadalupe island case study. *Journal of Geophysical Research: Atmospheres* **125** (4), e2019JD032121.

HUNT, J. & SNYDER, W. 1980 Experiments on stably and neutrally stratified flow over a model three-dimensional hill. *Journal of Fluid Mechanics* **96** (4), 671–704.

JAGANNATHAN, A., SRINIVASAN, K., MCWILLIAMS, J. C., MOLEMAKER, M. J. & STEWART, A. L. 2021 Boundary-layer-mediated vorticity generation in currents over sloping bathymetry. *Journal of Physical Oceanography* **51** (6), 1757–1778.

KLOOSTERZIEL, R. & VAN HEIJST, G. 1991 An experimental study of unstable barotropic vortices in a rotating fluid. *Journal of Fluid Mechanics* **223**, 1–24.

KUMAR, B. & MITTAL, S. 2006 Effect of blockage on critical parameters for flow past a circular cylinder. *International Journal for Numerical Methods in Fluids* **50** (8), 987–1001.

KUMAR, B. & MITTAL, S. 2012 On the origin of the secondary vortex street. *Journal of Fluid Mechanics* **711**, 641–666.

LAZAR, A., STEGNER, A. & HEIFETZ, E. 2013*a* Inertial instability of intense stratified anticyclones. Part 1. generalized stability criterion. *Journal of Fluid Mechanics* **732**, 457–484.

LAZAR, A., STEGNER, A. & HEIFETZ, E. 2013*b* Inertial instability of intense stratified anticyclones. Part 2. laboratory experiments. *Journal of Fluid Mechanics* **732**, 485–509.

LIU, C.-L. & CHANG, M.-H. 2018 Numerical studies of submesoscale island wakes in the Kuroshio. *Journal of Geophysical Research: Oceans* **123** (8), 5669–5687.

LUMLEY, J. L. 1967 The structure of inhomogeneous turbulent flows. *Atmospheric Turbulence and Radio Wave Propagation* pp. 166–178.

LUMLEY, J. L. 1970 *Stochastic Tools in Turbulence*. Academic Press.

MACKINNON, J. A., ALFORD, M. H., VOET, G., ZEIDEN, K. L., SHAUN JOHNSTON, T., SIEGELMAN, M., MERRIFIELD, S. & MERRIFIELD, M. 2019 Eddy wake generation from broadband currents near Palau. *Journal of Geophysical Research: Oceans* **124** (7), 4891–4903.

MARSHALL, J., ADCROFT, A., HILL, C., PERELMAN, L. & HEISEY, C. 1997*a* A finite-volume, incompressible Navier-Stokes model for studies of the ocean on parallel computers. *Journal of Geophysical Research: Oceans* **102** (C3), 5753–5766.

MARSHALL, J., HILL, C., PERELMAN, L. & ADCROFT, A. 1997*b* Hydrostatic, quasi-hydrostatic, and nonhydrostatic ocean modeling. *Journal of Geophysical Research: Oceans* **102** (C3), 5733–5752.

MITTAL, S. 2008 Global linear stability analysis of time-averaged flows. *International Journal for Numerical Methods in Fluids* **58** (1), 111–118.

MUTABAZI, I., NORMAND, C. & WESFREID, J. E. 1992 Gap size effects on centrifugally and rotationally driven instabilities. *Physics of Fluids A: Fluid Dynamics* **4** (6), 1199–1205.

NICOUD, F. & DUCROS, F. 1999 Subgrid-scale stress modelling based on the square of the velocity gradient tensor. *Flow, Turbulence and Combustion* **62** (3), 183–200.

NIDHAN, S., CHONGSIRIPINYO, K., SCHMIDT, O. T. & SARKAR, S. 2020 Spectral proper orthogonal decomposition analysis of the turbulent wake of a disk at $Re = 50000$. *Physical Review Fluids* **5** (12), 124606.

NIDHAN, S., SCHMIDT, O. T. & SARKAR, S. 2022 Analysis of coherence in turbulent stratified wakes using spectral proper orthogonal decomposition. *Journal of Fluid Mechanics* **934**.

NOACK, B. R., AFANASIEV, K., MORZYŃSKI, M., TADMOR, G. & THIELE, F. 2003 A hierarchy of low-dimensional models for the transient and post-transient cylinder wake. *Journal of Fluid Mechanics* **497**, 335–363.

ORTIZ-TARIN, J. L., NIDHAN, S. & SARKAR, S. 2023 The high-Reynolds-number stratified wake of a slender body and its comparison with a bluff-body wake. *Journal of Fluid Mechanics* **957**, A7.

PAWLAK, G., MACCREADY, P., EDWARDS, K. & MCCABE, R. 2003 Observations on the evolution of tidal vorticity at a stratified deep water headland. *Geophysical Research Letters* **30** (24).

PERFECT, B. 2019 The energetics and vortex structure of seamounts in stratified, rotating flow. PhD thesis, University of Washington.

PERFECT, B., KUMAR, N. & RILEY, J. 2018 Vortex structures in the wake of an idealized seamount in rotating, stratified flow. *Geophysical Research Letters* **45** (17), 9098–9105.

PUTHAN, P., JALALI, M., ORTIZ-TARIN, J. L., CHONGSIRIPINYO, K., PAWLAK, G. & SARKAR, S. 2020 The wake of a three-dimensional underwater obstacle: Effect of bottom boundary conditions. *Ocean Modelling* **149**, 101611.

PUTHAN, P., PAWLAK, G. & SARKAR, S. 2022*a* High drag states in tidally modulated stratified wakes. *Journal of Physical Oceanography* **52** (6), 1033–1048.

PUTHAN, P., PAWLAK, G. & SARKAR, S. 2022*b* Wake vortices and dissipation in a tidally modulated flow past a three-dimensional topography. *Journal of Geophysical Research: Oceans* **127** (8), e2022JC018470.

Puthan, P., Sarkar, S. & Pawlak, G. 2021 Tidal synchronization of lee vortices in geophysical wakes. *Geophysical Research Letters* **48** (4), e2020GL090905.

Rapaka, N. R. & Sarkar, S. 2016 An immersed boundary method for direct and large eddy simulation of stratified flows in complex geometry. *Journal of Computational Physics* **322**, 511–534.

Rayleigh, L. 1917 On the dynamics of revolving fluids. *Proceedings of the Royal Society of London. Series A, Containing Papers of a Mathematical and Physical Character* **93** (648), 148–154.

Rempfer, D. & Fasel, H. F. 1994 Evolution of three-dimensional coherent structures in a flat-plate boundary layer. *Journal of Fluid Mechanics* **260**, 351–375.

Schmidt, O. T. & Colonius, T. 2020 Guide to spectral proper orthogonal decomposition. *AIAA Journal* **58** (3), 1023–1033.

Shchepetkin, A. F. & McWilliams, J. C. 2005 The regional oceanic modeling system (ROMS): a split-explicit, free-surface, topography-following-coordinate oceanic model. *Ocean Modelling* **9** (4), 347–404.

Sirovich, L. 1987 Turbulence and the dynamics of coherent structures. I. coherent structures. *Quarterly of Applied Mathematics* **45** (3), 561–571.

Spedding, G. 1997 The evolution of initially turbulent bluff-body wakes at high internal Froude number. *Journal of Fluid Mechanics* **337**, 283–301.

Srinivasan, K., McWilliams, J. C. & Jagannathan, A. 2021 High vertical shear and dissipation in equatorial topographic wakes. *Journal of Physical Oceanography* **51** (6), 1985–2001.

de Stadler, M. B. & Sarkar, S. 2012 Simulation of a propelled wake with moderate excess momentum in a stratified fluid. *Journal of Fluid Mechanics* **692**, 28–52.

Taylor, J. R. & Sarkar, S. 2008 Stratification effects in a bottom Ekman layer. *Journal of Physical Oceanography* **38** (11), 2535–2555.

Taylor, J. R. & Thompson, A. F. 2023 Submesoscale dynamics in the upper ocean. *Annual Review of Fluid Mechanics* **55**.

Teinturier, S., Stegner, A., Didelle, H. & Viboud, S. 2010 Small-scale instabilities of an island wake flow in a rotating shallow-water layer. *Dynamics of Atmospheres and Oceans* **49** (1), 1–24.

Towne, A., Schmidt, O. T. & Colonius, T. 2018 Spectral proper orthogonal decomposition and its relationship to dynamic mode decomposition and resolvent analysis. *Journal of Fluid Mechanics* **847**, 821–867.

VanDine, A., Chongsiripinyo, K. & Sarkar, S. 2018 Hybrid spatially-evolving DNS model of flow past a sphere. *Computers & Fluids* **171**, 41–52.

Vosper, S., Castro, I., Snyder, W. & Mobbs, S. 1999 Experimental studies of strongly stratified flow past three-dimensional orography. *Journal of Fluid Mechanics* **390**, 223–249.

Welch, P. 1967 The use of fast Fourier transform for the estimation of power spectra: a method based on time averaging over short, modified periodograms. *IEEE Transactions on Audio and Electroacoustics* **15** (2), 70–73.

Williamson, C. & Brown, G. 1998 A series in $1/\sqrt{Re}$ to represent the Strouhal-Reynolds number relationship of the cylinder wake. *Journal of Fluids and Structures* **12** (8), 1073–1085.

Yang, J. & Balaras, E. 2006 An embedded-boundary formulation for large-eddy simulation of turbulent flows interacting with moving boundaries. *Journal of Computational Physics* **215** (1), 12–40.

Yim, E., Billant, P. & Ménesguen, C. 2016 Stability of an isolated pancake vortex in continuously stratified-rotating fluids. *Journal of Fluid Mechanics* **801**, 508–553.

Yim, E., Stegner, A. & Billant, P. 2019 Stability criterion for the centrifugal instability of surface intensified anticyclones. *Journal of Physical Oceanography* **49** (3), 827–849.

Young, G. S. & Zawislak, J. 2006 An observational study of vortex spacing in island wake vortex streets. *Monthly Weather Review* **134** (8), 2285–2294.

Zeiden, K. L., MacKinnon, J. A., Alford, M. H., Rudnick, D. L., Voet, G. & Wijesekera, H. 2021 Broadband submesoscale vorticity generated by flow around an island. *Journal of Physical Oceanography* **51** (4), 1301–1317.

Zhou, Y. & Antonia, R. 1992 Convection velocity measurements in a cylinder wake. *Experiments in Fluids* **13** (1), 63–70.